Astronomy & Astrophysics manuscript no. output
September 10, 2021

Spectral modelling of Type IIb Supernovae.

Comparison to SN 2011dh and the effect of macroscopic mixing.

M. Ergon[1] and C. Fransson[1]

The Oskar Klein Centre, Department of Astronomy, AlbaNova, Stockholm University, 106 91 Stockholm, Sweden

To be submitted to Astronomy and Astrophysics.

ABSTRACT

We use the new NLTE spectral synthesis code JEKYLL to evolve a macroscopically mixed ejecta model of a type IIb SN **originating from a star with an initial mass of 12 $M_{\odot}$** through the photospheric and nebular phase. We compare to SN 2011dh, and find that both the spectra and the lightcurves are well reproduced in both the photospheric and nebular phase, although there are also some differences. Our work complement and advance earlier work on SN 2011dh, and further strengthens the evidence that this SN originated from a **star with an initial mass of** $\sim$12 $M_{\odot}$. In preparation for JWST we present infrared model spectra, demonstrating the usefulness of these for abundance determinations. We also investigate the effects of the macroscopic mixing by comparing macroscopically and microscopically mixed models, and by varying the clumping geometry, which is determined by the expansion of clumps containing radioactive material and the typical sizes of the clumps. In the nebular phase, we find strong effects on the collisional cooling rates in the macroscopically mixed regions, which affects the strength of lines driven by collisional cooling, in particular, the [Ca II] 7291,7323 Å lines, the Ca II triplet and the [O I] 6300,6364 Å lines. In the photospheric phase, we find strong effects on the opacity in the macroscopically mixed regions, which affects the observed lightcurves. The diffusion peak is considerably narrower in the macroscopically mixed case, and differs strongly if the clumps containing radioactive material in the helium envelope are assumed to expand more than in our standard model. The effect is mainly geometrical, and is driven by the expansion of the clumps containing radioactive material. **If the** radiation field **is independent of the clump type**, this tends to decrease the effective opacity, and in the limit of optically thick clumps, the decrease is roughly given by the product of the filling factor and the **(volume)** expansion factor. The effect also depends on the typical size of the clumps, as the geometrical part disappears when the clumps becomes optically thin. Our findings has implications for lightcurve modelling of stripped-envelope SNe in general, and the effect will tend to increase the estimated ejecta masses. As shown in this and earlier work, *both* NLTE and macroscopic mixing are essential ingredients to reproduce the lightcurves and spectra of Type IIb SNe throughout their evolution.

Key words. supernovae: general

1. Introduction

Type IIb SNe are thought to originate from stars that have lost most, but not all of their hydrogen envelope. Except for the prototypical Type IIb SN 1993J, the most well-observed Type IIb SN is 2011dh, for which we presented observations and modelling of the lightcurves in Ergon et al. (2014, 2015, hereafter E14, E15), as well as modelling of nebular spectra in Jerkstrand et al. (2015, hereafter J15). The modelling suggested an initial mass of $\sim$12 $M_{\odot}$ for the progenitor, a conclusion supported by observations of the star in pre-explosion images (Maund et al. 2011). As stellar winds for stars of this mass seem too low to expel the hydrogen envelope this suggests a binary origin, where the hydrogen envelope was lost through interaction with a companion star. A similar conclusion applies to SN 1993J, based on modelling of the SN (Shigeyama et al. 1994; Woosley et al. 1994), pre-explosion observations of the progenitor star (Aldering et al. 1994), as well as a likely post-explosion detection of the companion star (Maund et al. 2004; Fox et al. 2014). We also studied a large sample of Type IIb SNe using a grid of hydrodynamical models in Ergon (2015), where we found most of those to originate from relatively low-mass stars. However, the simplified treatment of the opacity in the hydrodynamical modelling, makes this result somewhat uncertain.

Mixing of the SN ejecta occurs in the explosion due to hydrodynamical instabilities (e.g. Mueller et al. 1991). Hydrodynamical modelling suggests that the mixing is extensive in Type IIb SNe (Wongwathanarat et al. 2017), a conclusion that is supported by observations (e.g. E15). In addition, both theoretical arguments (e.g. Fryxell et al. 1991), and observations (e.g. Ennis et al. 2006) suggests that it occurs on macroscopic scales only. Such *macroscopic mixing* is purely geometrical, **and is facilitated through fragmentation of the ejecta into clumps, in which** the composition remains intact. This in contrast to *microscopic mixing*, which occurs on microscopic scales, e.g. through diffusion or turbulence. In traditional 1-D codes, macroscopic mixing can not be simulated **(Is this really true?)**. In that case the choice is to either ignore the mixing or assume that it is microscopic. On the other hand, in MC-based 1-D codes it is possible to simulate macroscopic mixing in a statistical way, e.g. by using the virtual **grid** method (Jerkstrand et al. 2011, hereafter J11), which allows for a statistical representation of ejecta consisting of clumps of different composition. JEKYLL supports the virtual **grid** method, and we can therefore take the macroscopic mixing of the ejecta into account, and investigate the effects of it. Note, that the clumping geometry is not only determined by the fragmentation and mixing that occurs in the explosion, but also by the subsequent expansion of clumps containing radioactive material due to heating from radioactive decays (e.g Herant & Benz 1991).

In (Ergon et al. 2018, hereafter Paper I) we presented, described and tested JEKYLL, and discussed the effect of NLTE on the spectra and lightcurves of a microscopically mixed Type IIb model. In this paper we use JEKYLL to evolve a macroscopically mixed Type IIb model through the photospheric and nebular phase. This model belongs to a set of models that was earlier evolved through the nebular phase using SUMO (J11), and compared to the observed nebular spectra and lightcurves of SN 2011dh in J15 and E15, respectively. Out of those, the strongly mixed 12 $M_{\odot}$ model explored here, showed the best agreement with the nebular spectra and lightcurves of SN 2011dh. It is therefore of great interest to investigate how well this model compares to the spectra and lightcurves of SN 2011dh in the photospheric phase, which is the first objective of this paper. The second objective is to investigate the effects of the macroscopic mixing on the result, and we have therefore constructed a microscopically mixed version of the model, and a set of macroscopically mixed models differing in the clumping geometry. In our treatment, the clumping geometry is determined by the sizes of the clumps and their filling factors (the total volume they occupy). The filling factors are in turn determined by the expansion of the clumps containing radioactive material, which creates a density contrast between these and other clumps.

The paper is organized as follows. In Sect. 2 we describe the methods used and our set of models, in Sect. 3 we discuss the modelling results for our standard model, and compare to observations of SN 2011dh, and in Sect. 4 we investigate the effect of macroscopic mixing on the modelling results. Finally, in Sect. 5 we conclude and summarize the paper.

2. Methods and models

All SN models presented in this work were calculated with the JEKYLL code, which was described in detail in Paper I. Here, we briefly repeat the general methods used in JEKYLL, and discuss the treatment of the macroscopic mixing in some more detail. In addition, we describe the set-up of JEKYLL, the atomic data and the initial conditions used to evolve the SN models through the photospheric and nebular phase.

The SN models are based on **the** Type IIb ejecta model **12C** from the set presented by J15, which corresponds to a progenitor star with an initial mass of 12 $M_{\odot}$ and strong macroscopic mixing of the ejecta. Based on this ejecta model, we construct a standard model, which differs slightly from the original one, and a set of models that differs in the type of mixing (macroscopic or microscopic) and the clumping geometry.

2.1. General methods

JEKYLL is a spectral-synthesis code based on a Monte-Carlo (MC) method for the time-dependent radiative transfer developed by Lucy (2002, 2003, 2005), and extended as described in Paper I. To calculate the radiation field and the state of matter[1] an iterative procedure is used, where these are determined from each other. JEKYLL has several solvers to calculate the state of matter, but here we use the NLTE solver, where the statistical and thermal equilibrium equations are solved for taking into account all relevant processes. In particular, this includes heating, excitation and ionization by non-thermal electrons calculated using the method by Kozma & Fransson (1992). In the inner region, where the matter and radiation field are assumed to be coupled, we use a diffusion solver to calculate the temperature. The main limitations in JEKYLL are the assumptions of homologous expansion, **thermal and statistical equilibrium,** and spherical symmetry. The latter is, however, only assumed on average, as we discuss in the next section.

2.2. Treatment of the macroscopic mixing

To simulate the macroscopic mixing JEKYLL use the virtual cell **grid** method (J11). The ejecta are assumed to be spherically symmetric on average, and the macroscopic mixing is represented by distinct types of spherical clumps, characterized by their composition, density, size and filling factor. In the MC radiative transfer, the clumps are drawn based on their geometrical cross-section as the MC packets propagates through a macroscopically mixed region. This means that each MC packet sees a different geometrical arrangement of the clumps, which is justified in the limit of many clumps. The state of matter is calculated separately for each type of clumps using a MC radiation field constructed from MC packets passing through these clumps. The internal stratification of the **state of matter** (but not the radiation field) in the clumps is ignored. In the inner region, where we use the diffusion solver, we assume a uniform temperature and use an effective Rosseland mean opacity (see Sect. 4.2 and Appendix A), but otherwise calculate the **state of matter** separately for each type of clumps. Note, that the MC radiative transfer for the γ-rays emitted in the radioactive decays uses the virtual **grid** method both in the inner and outer region.

Clearly, the virtual **grid** method is a simplification, and might be considered as a convenient parametrization of the more general 3-D problem. Although it would be possible to map a 3-D hydrodynamical simulation to this parametrization (and we may explore that path in the future), the models explored here are based on 1-D hydrodynamical simulations, where the compositional layers have been artificially mixed **with** each-other. In this work we do not explore the extent of the mixing, but focus on the type of mixing (macroscopic or microscopic) and the clumping geometry. Given the mass-fractions of the compositional layers in a macroscopically mixed region, the clumping geometry is determined by the sizes and the filling factors of the clumps. These are in turn determined by the original sizes of the clumps and the expansion of the clumps containing radioactive material, which results in a corresponding compression of the other clumps. The sizes and the filling factors of the clumps in our models are discussed in Sect. 2.5. **In this paper we parametrize this expansion, and study the sensitivity of our results to different assumptions.**

As JEKYLL is not hydrodynamical, we assume that all important hydrodynamical effects occurred before the start of the simulation. This assumption is safe with respect to the fragmentation of the ejecta into clumps, which occurs in the explosion, but less so for the subsequent expansion of the clumps containing radioactive material. At early times, the decay energy is deposited locally, and if the diffusion timescale is long compared to the decay and expansion timescales, this creates a temperature difference. If, in addition, the hydrodynamical timescale is small compared to the diffusion timescale, the corresponding pressure difference drives an expansion of the clumps. This means that we are on the safe side if the diffusion timescale is small compared to the decay and expansion timescales. Fortunately, in all our models, the diffusion time in the clumps never exceeds ~3 days in the core and ~0.5 days in the envelope, so after a few

[1] With state of matter we refer to the temperature and the populations of ionized and excited states.

days this condition is increasingly well fulfilled. **Nevertheless, the homologeous assumption introduces an uncertainty during the first weeks.**

2.3. Set-up

JEKYLL was set up to run in time-dependent mode (with respect to the radiative transfer), and to use a full NLTE solution including the following; radiative bound-bound, bound-free and free-free processes, collisional bound-bound and bound-free processes, non-thermal excitation, ionization and heating, as well as two-photon processes. **We use the diffusion** solver below an optical depth of 50, and a recombination correction **explain!** while still enforcing detailed balance. In addition, packet control (Paper I) was turned on to assure good sampling of the radiation field in all frequency regions. The logarithmic **increase of the** time-step was set to 5 percent and the number of Λ-iterations per time-step was set to 4. As discussed in Paper I, this gives a well converged solution, which has also been verified for the models used in this paper.

2.4. Atomic data

The atomic data used is the default choice described in Paper I, but has been extended with more levels and a full NLTE solution for ionization stages V and VI. This makes only a small difference for the observed lightcurves and spectra, but is needed to study the opacity in the macroscopically mixed core, which becomes very hot **more specific?** $\sim 10^5$ **K?** at early times. Using online data provided by NIST[2] and R. Kurucz[3], these ions where updated to include 100 levels (or as many as were available) for elements lighter than Scandium and 300 levels (or as many as were available) for heavier elements. Total recombination rates for these ions were adopted from the online table provided by S. Nahar[4] whenever available, and otherwise from Shull & van Steenberg (1982).

2.5. Ejecta models

A full description of **the Type IIb** model 12C is given in J15, but we repeat the basic properties here. It is based on a SN model by Woosley & Heger (2007) for a star with an initial mass of 12 $M_{\odot}$, from which the masses and abundances for the carbon-oxygen core and the helium envelope have been adopted. The carbon-oxygen core is assumed to have a constant (average) density, and the helium envelope to have the same (average) density profile as the best-fit model for SN 2011dh by Bersten et al. (2012). In addition, a 0.1 $M_{\odot}$ hydrogen envelope based on models by Woosley et al. (1994) is attached. The velocities of the interfaces between the carbon-oxygen core, the helium envelope and the hydrogen envelope are set to 3500 and 11000 km s^{-1}, respectively, based on observations of SN 2011dh.

Based on the original onion-like nuclear burning structure, J15 identified five compositional zones (O/C, O/Ne/Mg, O/Si/S, Si/S and **Ni/He**[5] in the carbon-oxygen core, two (He/N and He/C) in the helium envelope, and one (H) in the hydrogen envelope. To mimic the mixing of the compositional zones in the explosion, two scenarios with different degrees of mixing (medium and strong) were explored in J15. Model 12C has strong mixing, corresponding to a fully mixed carbon-oxygen core and about half of the radioactive **Ni/He** material mixed into the inner part of the helium envelope.

The treatment of the macroscopic mixing was discussed in Sect. 2.2, and given the mass-fractions of the compositional zones in a macroscopically mixed region, the clumping geometry is parametrized by the sizes and the filling factors of the clumps, or alternatively, by the original sizes of the clumps and the expansion of the clumps containing radioactive material. The constraints on these parameters are not very strong, but as discussed in J15, there are some observational constraints on the clumping geometry of the core, which were used as guidelines for the original model.

In Jerkstrand et al. (2012), a density contrast of ∼30 between the **Ni/He** and oxygen-rich clumps was derived for the Type IIP SN 2004et, and based on that a density contrast of 30 and 210 were explored in J15. Model 12C has a density contrast of 210, corresponding to an expansion factor[6] of 10 and a filling factor of 0.85 for the **Ni/He** clumps. In E15, a lower limit on the number of clumps in the O/Ne/Mg zone of ∼900 was derived from small-scale variations in the [O I] 6300,6364 and Mg I] 4571 Å line profiles of SN 2011dh, and based on that J15 assumed that each compositional zone in the core consisted of 10000 clumps.

For the comparison with SN 2011dh we have constructed a standard model, which is similar to model 12C. However, we have chosen to deviate in two aspects. First, we assume that all clumps have the same mass (instead of the same number per compositional zone), and second, we assume that the **Ni/He** clumps expand also in the helium envelope. The clump mass was chosen to give 5000 clumps in the O/Ne/Mg zone, and the expansion of the **Ni/He** clumps in the helium envelope was assumed to be half of that in the core. These assumptions seem more physically sound than the original ones, but the choices for the mass and expansion of the **Ni/He** clumps in the helium envelope are somewhat arbitrary. **Note, that our models does not include the simplified treatment of dust applied in J15, which might cause some differences after 150 days.**

To investigate the effect of the type of mixing, we have constructed a microscopically mixed version of the standard model by averaging the density and the abundances over the compositional zones. Similarly, to investigate the effect of the clumping geometry, we have constructed a set of models that differs in the expansion of the clumps containing radioactive material and the sizes of the clumps. These are; (1), a model where the **Ni/He** and Si/S clumps have not been expanded at all, (2), a model where the **Ni/He** clumps in the helium envelope have been expanded with a larger factor (8.5), and (3), a model where the number of clumps have been increased by a factor of 100. All models, and their parameters, are listed in Table 1.

2.6. Initial conditions

As for the HYDE models in E15, the initial temperature profile was taken from the best-fit hydrodynamical model for SN 2011dh from that paper. This SN model was based on a bare helium core model, and therefore the cooling of the thermal explosion energy, lasting for a few days in a model with a hydrogen envelope, is ignored. The subsequent evolution is powered by the continuous injection of radioactive decay energy, and the choice of initial temperature profile is not critical, although it may have some effect on the early evolution.

[2] www.nist.gov
[3] http://www.cfa.harvard.edu/amp/ampdata/kurucz23/sekur.html
[4] http://www.astronomy.ohio-state.edu/~nahar/_naharradiativeatomicdata/
[5] **Referred to as the Fe/Co/He zone in J15.**
[6] **Here and in the following this refers to the volume expansion factor.**

Table 1. Ejecta models.

Description	Type of mixing	**Ni/He** expansion core	**Ni/He** expansion envelope	Clump mass ($M_\odot$)
Standard model	macroscopic	10	5	8.4×10^{-6}
Microscopic mixing	microscopic	-	-	-
No expansion	macroscopic	1	1	8.4×10^{-6}
Stronger expansion	macroscopic	10	8.5	8.4×10^{-6}
More clumps	macroscopic	10	8.5	8.4×10^{-8}

3. Comparisons to observations

Among the Type IIb models presented in J15, model 12C, which has an initial mass of 12 $M_\odot$ and strong mixing was found to give the best match to the observed nebular spectra (J15) and lightcurves[7] (E15) of SN 2011dh. It is therefore of great interest to explore how well this model reproduces the early spectra and lightcurves, something which is now possible using JEKYLL. In addition, it is also interesting in itself to run a self-consistent model from the photospheric to the nebular phase. However, as the nebular phase was discussed in detail in J15, we mainly focus on on the first 150 days, which gives some overlap without being repetitive. Note, that in the comparison we use our standard version of model 12C, **which differs slightly from the original model (see Sect.2.2).**

In Sects. 3.2, 3.3, 3.4 and 3.5 we discuss the spectral, photometric, colour and bolometric evolution of the standard model and compare this to observations of SN 2011dh. First, however, we briefly discuss the evolution of the **state of matter** in the model, to provide some background for the discussion of the observed quantities that follows.

3.1. State of matter

Figure 1 shows the evolution of the temperature, electron fraction and radioactive energy deposition in the core, the inner/outer helium envelope and the hydrogen envelope for the standard model. These are averages over the spatial cells and the compositional zones, but in Sects. 4.1 and 4.3 we get back to this and discuss the variation of these quantities between the compositional zones. In Figure 1 we also show the evolution of the (Rosseland mean) continuum photosphere. Initially, the photosphere is at the border of the hydrogen envelope, which is relatively cool ($T \sim 5000$ K) and mainly recombined ($x_e \sim 0.2$) whereas the core is hot ($T \sim 50000$ K) and higly ionized ($x_e > 3$). Towards ~40 days, when the photosphere reaches the inner helium envelope, the temperature and the electron fraction in the inner parts decrease quickly, whereas the temperature begin to rise in the outer parts. After this the evolution slows down, the temperature continues to rise in the outer parts and exceeds 10000 K in the hydrogen envelope, whereas the electron fraction drops below 0.5 towards 100 days, roughly when the ejecta become optically thin in the continuum. The radioactive energy is initially deposited in the inner parts where the radioactive material resides, but at ~10 days the deposition begins to rise quickly in the outer parts, and we will get back to this issue below.

[7] The best match was found for model 12F, which differs from model 12C only in the optical depth of the dust.

3.2. Spectral evolution

Figures 2 and 3 show the spectral evolution for the standard model, where the former figure displays the radiative process, and the latter figure the location giving rise to the emission. In both cases this refers to the last emission/scattering events for the MC packets excluding electron scattering. Furthermore, in Fig. 4 we compare the spectral evolution in the optical and near-infrared (NIR) to observations of SN 2011dh. Note, that there are no NIR observations for SN 2011dh between ~100 and ~200 days.

As seen in Fig. 4, there is a good qualitative, and in many aspects also quantitative agreement, between the standard model and the observations of SN 2011dh. Before ~10 days, when the emission comes mainly from the hydrogen envelope the agreement is a bit worse (not shown). This is possibly an effect of the choice of initial conditions for the model (see Sect. 2.5), where the initial cooling of the explosion energy, lasting a few days, has been ignored. Another difference is the evolution redwards ~20000 Å, where a strong excess develops in the observed spectrum, beginning already at ~60 days. This excess was discussed in E15, and was attributed to dust formation in the ejecta.

The main signature of a Type IIb SN is the transition from a hydrogen to a helium dominated spectrum, and this is well reproduced by the model. Initially, the hydrogen lines are strong and emission from the hydrogen envelope is dominating. Already at ~10 days emission from the helium envelope starts to dominate redwards ~5000 Å, and between 10 and 15 days the helium lines appear, grow stronger, and eventually dominate the spectrum at ~40 days. Hydrogen line emission disappears on a similar time-scale, completing the transition, although the Balmer lines remain considerably longer in absorption. The first 40 days is also the period over which the contribution from continuum processes fades away. Initially, this contribution is substantial redwards ~5000 Å and dominating in the NIR, but then quickly fades away, although it remains important in the H-band and redwards 23000 Å until ~40 days.

After ~40 days, emission from the carbon-oxygen core becomes increasingly important and at ~100 days it dominates redwards ~5000 Å. As a consequence, emission from heavier elements abundant in the core increases, in particular after ~100 days, when the characteristic [O I] 6300,6364 Å and [Ca II] 7291,7323 Å lines appear. This is also the moment when the carbon-oxygen core becomes fully transparent in the continuum (see Fig.1), and therefore marks the transition into the nebular phase. This transition, in itself a demanding test of the code, is nicely reproduced by the model. As discussed in Sect. 4, this is partly due to our treatment of the macroscopic mixing.

Below, we discuss the most important lines originating from the different elements in some detail (Sects. 3.2.1-3.2.5), as well as the line velocities measured from their absorption minima (Sect. 3.2.7), and again compare to observations of SN 2011dh.

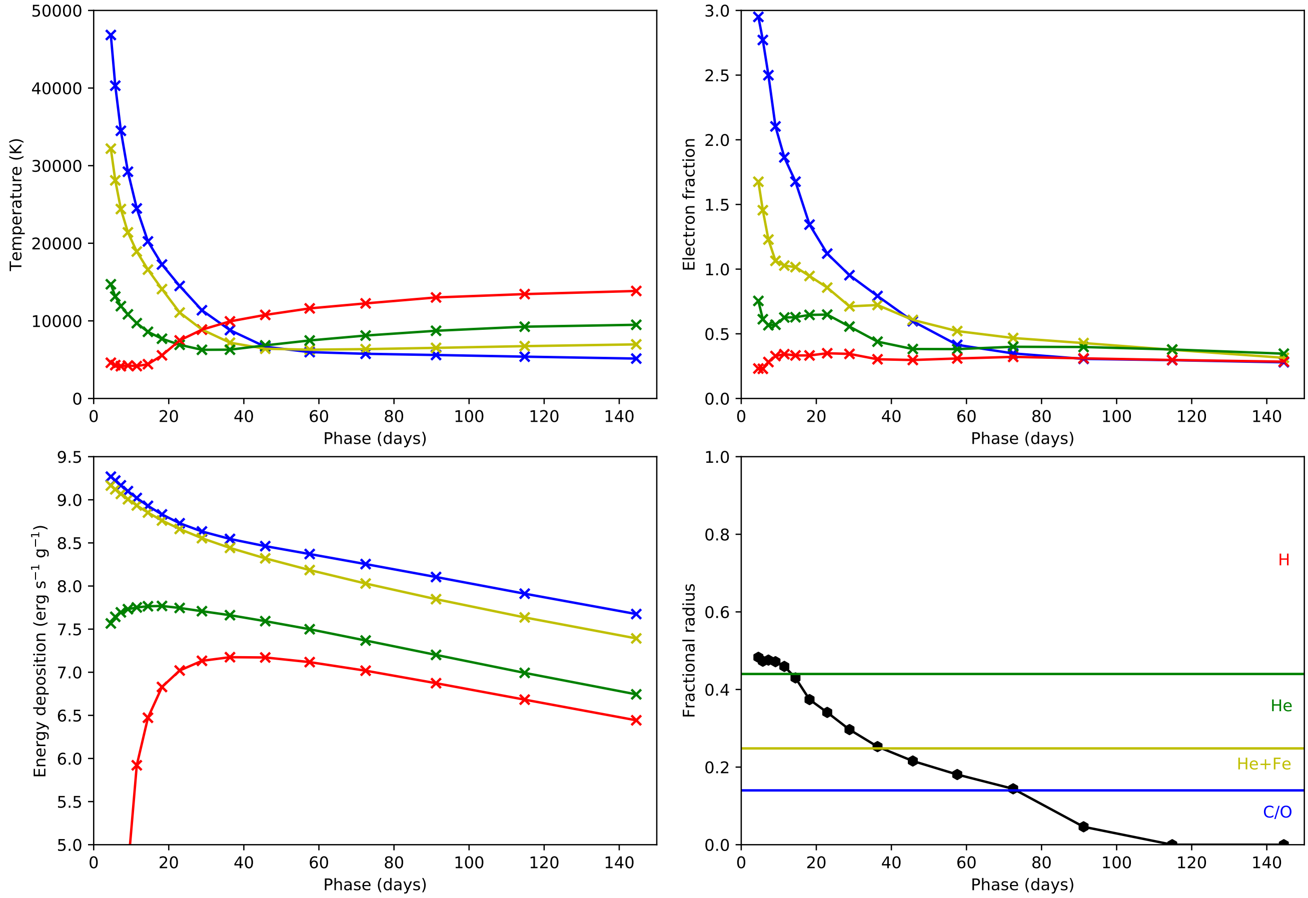

Fig. 1. Evolution of the temperature (upper left panel), electron fraction (upper right panel) and radioactive energy deposition (lower left panel) in the oxygen core (blue), inner/outer (yellow/green) helium envelope and the hydrogen envelope (red) for the standard model. In the lower right panel we show the evolution of the (Rosseland mean) continuum photosphere (black) as well as the outer borders of the carbon-oxygen core (blue) and inner/outer (green/yellow) helium envelope.

3.2.1. Hydrogen

The contribution from hydrogen lines is shown in Fig. 2, and as mentioned it is initially strong, but fades away after ∼10 days, when the photosphere retreats into the increasingly transparent helium envelope (see Fig. 1). This trend is most pronounced for the recombination driven Paschen lines, which disappear towards ∼40 days. Balmer line emission fades on a similar timescale, whereas absorption remains for a longer time, and even increases before ∼40 days. Contrary to the other Balmer lines, Hα initially shows a clear P-Cygni profile, but after ∼10 days it becomes increasingly blended with the He I 6678 Å line and attains the double-peaked shape so characteristic in Type IIb SNe.

Figure 5 shows the evolution of the Balmer lines compared to SN 2011dh. The evolution is qualitatively similar, but the absorption is significantly stronger and remains longer in the model, suggesting that the ∼0.05 $M_{\odot}$ of hydrogen in the model is larger than for SN 2011dh. This is in line with the 0.02-0.04 and 0.024 $M_{\odot}$ of hydrogen estimated through spectral modelling of SN 2011dh by E14[8] and Marion et al. (2014), respectively. In agreement with the spectral modelling in E14, we also find that the absorption minimum of the Balmer lines asymptotically approaches the velocity of the helium/hydrogen envelope interface. The Type IIb models by Dessart et al. (2015, 2016) behave in a similar way, and a stagnation of the absorption velocity for the Balmer lines is observed in most Type IIb SNe (see e.g. Liu et al. 2016). The stagnation velocity varies among different SNe, and for the most well-observed Type IIb SNe 1993J, 2011dh and 2008ax it is ∼9000, ∼11000 and ∼13000 km s^{-1} respectively, suggesting progressively lower hydrogen masses for these SNe (E14).

[8] Using an early version of JEKYLL assuming steady-state, LTE and (electron and line) scattering only.

3.2.2. Helium

The contribution from helium lines is shown in Fig. 2, and as mentioned, it increases strongly between 10 and 15 days, dominates the spectrum between 20 and 60 days and thereafter fades away in the optical, but remains important in the NIR. As demonstrated by Lucy (1991), non-thermal excitation and ionization are essential to populate the excited levels of He I, in turn required to produce the lines observed. This was confirmed by Dessart et al. (2012), and in Paper I we showed that if the non-thermal excitation and ionization were turned off in a microscopically mixed version of the model explored here, the helium lines disappeared.

Figure 6 shows the evolution of the He I 5876 Å, 6678 Å, 7065 Å, 10830 Å, 17007 Å and 20581 Å lines compared to SN 2011dh. These are the lines that stand out most clearly in the model, but several other weaker and blended lines like the He I 3890 Å, 4714 Å, 5017 Å and 7283 Å lines are also present. The

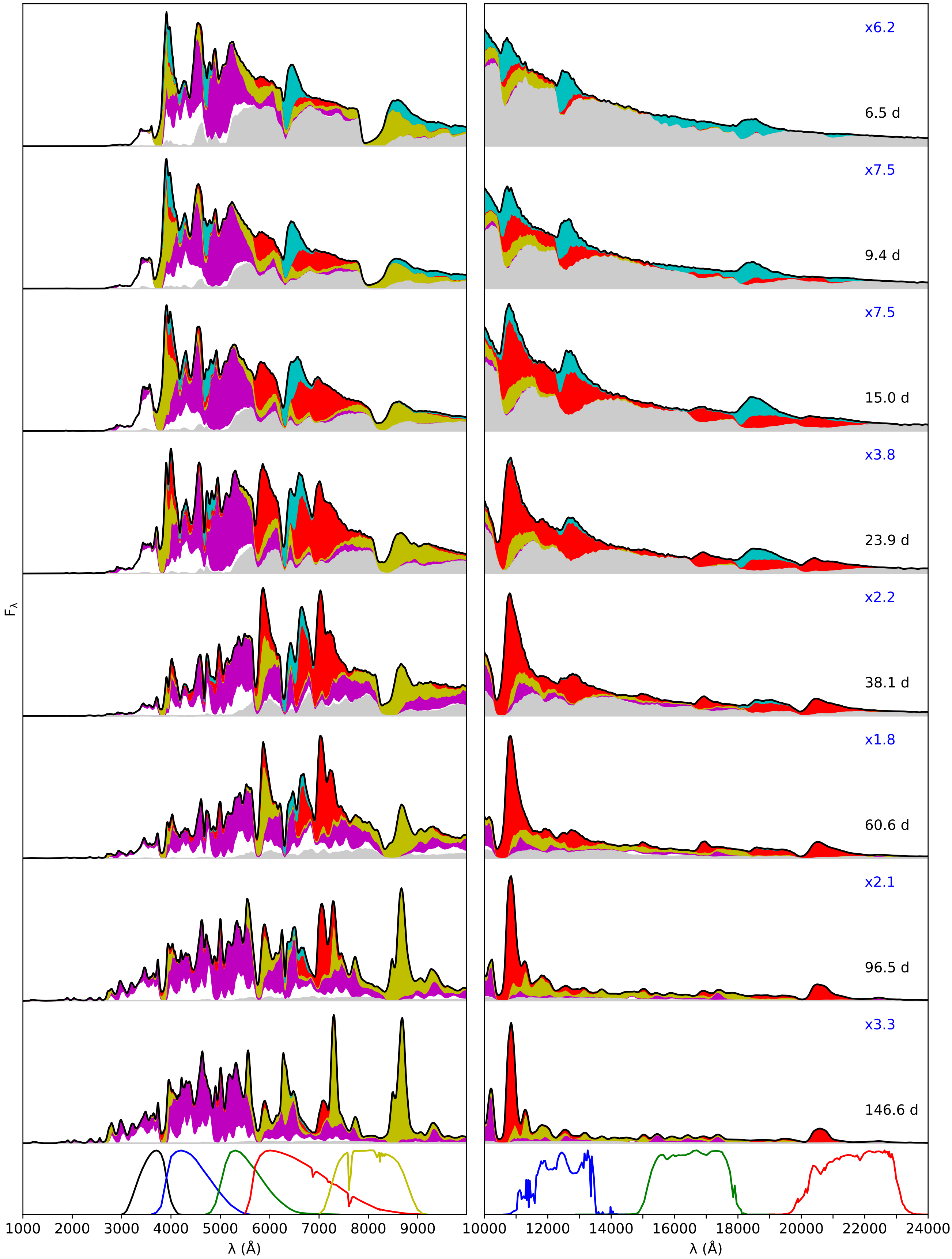

Fig. 2. Spectral evolution in the optical (left panel) and NIR (right panel) for the standard model, where the NIR flux has been scaled as indicated in blue. In the spectra we show the contributions to the emission from bound-bound transitions of hydrogen (cyan), helium (red), **carbon to calcium etc.** carbon-calcium (yellow), scandium-manganese (white) and iron-nickel (magenta) as well as continuum processes (grey). At the bottom we show the transmission profiles of the optical Johnson-Cousins *U* (black), *B* (blue), *V* (green), *R* (red) and *I* (yellow) bands and the NIR 2MASS *J* (blue), *H* (green) and *K* (red) bands.

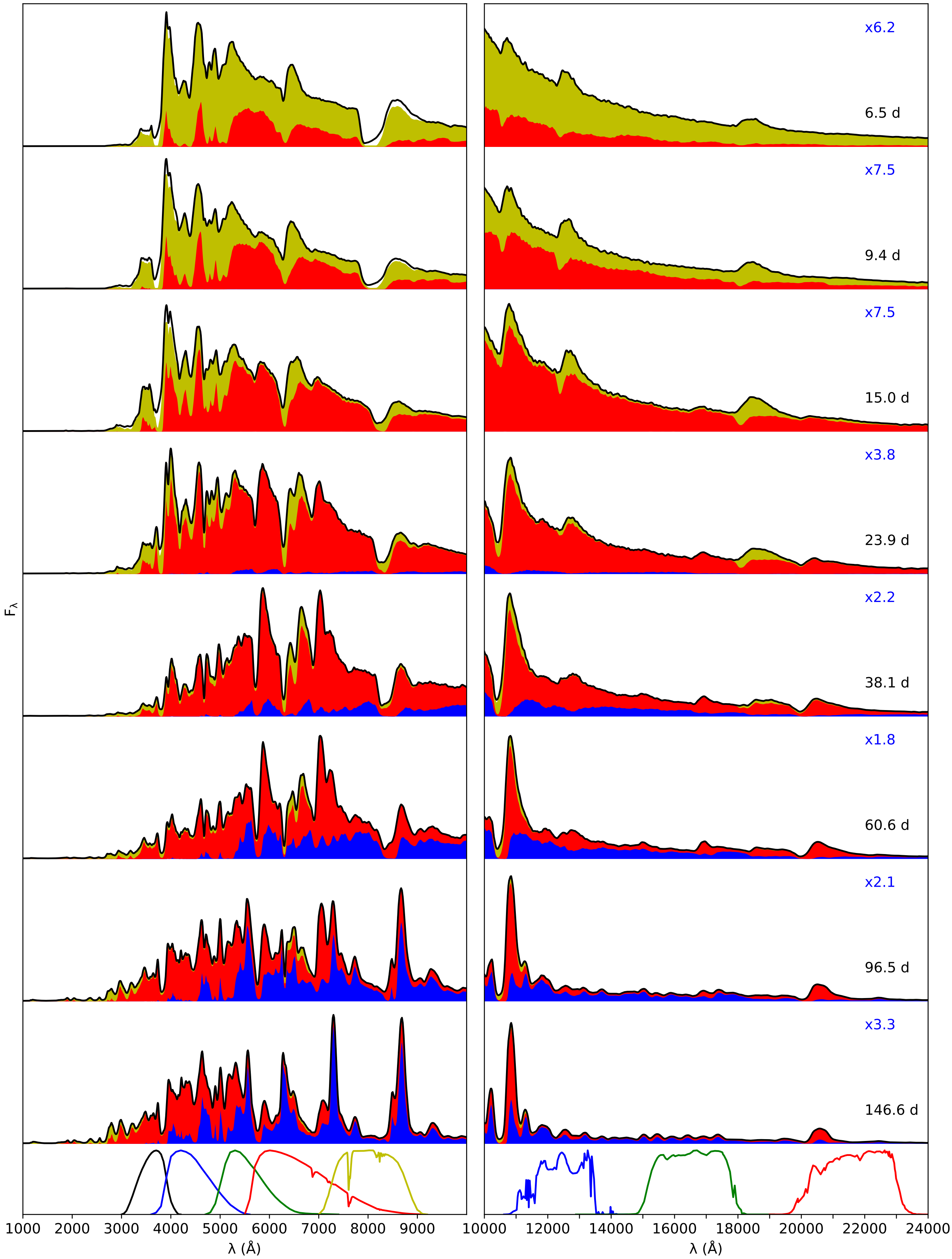

Fig. 3. Spectral evolution in the optical (left panel) and NIR (right panel) for the standard model, where the NIR flux has been scaled as indicated in blue. In the spectra we show the contributions to the emission from the carbon-oxygen core (blue), and the helium (red) and hydrogen (yellow) envelopes. At the bottom we show the transmission profiles of the optical Johnson-Cousins *U* (black), *B* (blue), *V* (green), *R* (red) and *I* (yellow) bands and the NIR 2MASS *J* (blue), *H* (green) and *K* (red) bands.

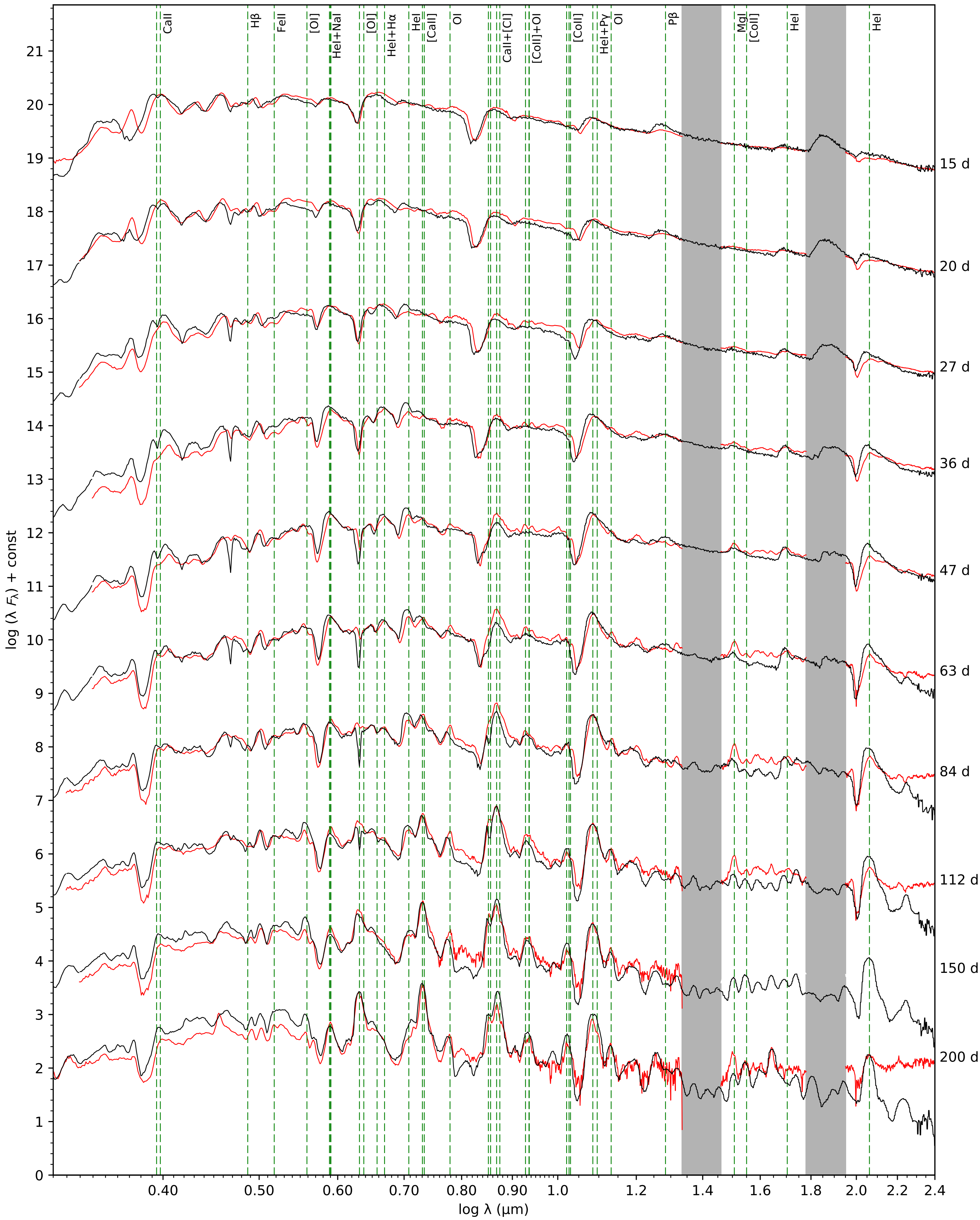

Fig. 4. Spectral evolution for the standard model (black) compared to the observations of SN 2011dh (red). Spectra from 10 equally spaced epochs between 15 and 200 days are shown. Here, and in the following figures the spectra of SN 2011dh have been interpolated as described in E14, but we only show interpolations that have an observational counterpart close in time. In addition, the rest-wavelengths of the most important lines are shown as red dashed lines and the NIR telluric absorption bands as grey vertical bars.

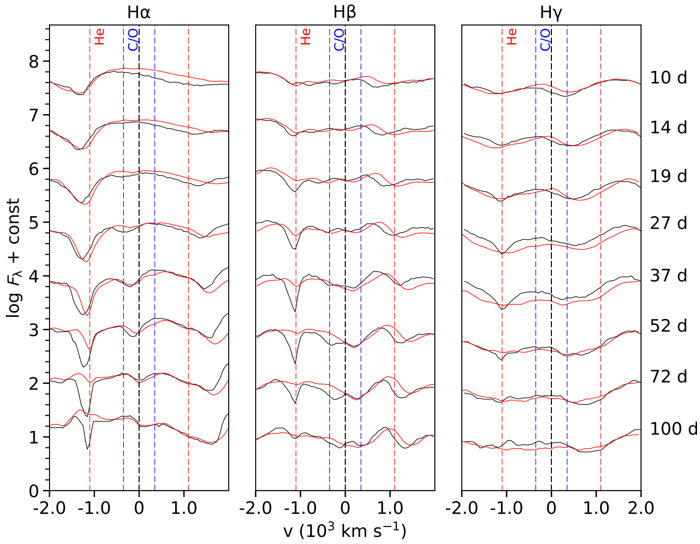

Fig. 5. Evolution of hydrogen lines for the standard model (black) compared to the observations of SN 2011dh (red). Spectra from 8 logarithmically spaced epochs between 10 and 100 days are shown. Here, as well as in Figs. 6-9, we also show the velocity extent of the helium envelope (red lines) and the carbon-oxygen core (blue lines).

He I 5876 Å, 6678 Å and 10830 Å lines are quite well reproduced by the model, whereas the He I 7065 Å and 20581 Å lines are overproduced in emission, and the weaker He I 17007 Å line (mainly seen in emission) is considerably stronger than in the observed spectra. The P-Cygni profiles for most of the helium lines are shifted towards higher velocities than observed, most pronounced at early times and in the 7065 Å and 20581 Å lines. These differences could indicate that too much Ni/He material has been mixed into the helium envelope in the model, or that the helium-rich clumps are more compressed than in our standard scenario. This would decrease the ionization and diminish the recombination contribution. Note, that after ~50 days most of the He I 5876 Å line emission is scattered by the Na I 5890,5896 Å lines.

As seen in Fig. 6, the He I 10830 Å absorption migrates outward in velocity until ~40 days, a behaviour repeated to some degree by the He I 20581 Å line. This behaviour is also observed in SN 2011dh, although in that case the optical helium lines showed a similar, but less pronounced trend. In E14 we suggested that the evolution of the helium lines is driven mainly by the ejecta becoming optically thin to the γ-rays. This idea is supported by Fig. 7, which shows the evolution of the radioactive energy deposition in the helium envelope. Between 10 and 15 days there is a strong increase in the energy deposition outside the photosphere, corresponding well to the period when the helium lines appear and grow in strength. We also see that the energy deposition in the outermost helium layers continues to increase to ~40 days, which may explain the evolution of the He I 10830 Å line. The outward migration of the He I 10830 Å absorption is also present in the Type I/IIb models (e.g. model 3p65Ax1) by Dessart et al. (2015, 2016), and was noted and discussed by the authors, who also provide a similar explanation.

3.2.3. Carbon to calcium

The (line) contribution from elements in the carbon to calcium range is shown in Fig. 2, and except for the calcium lines which

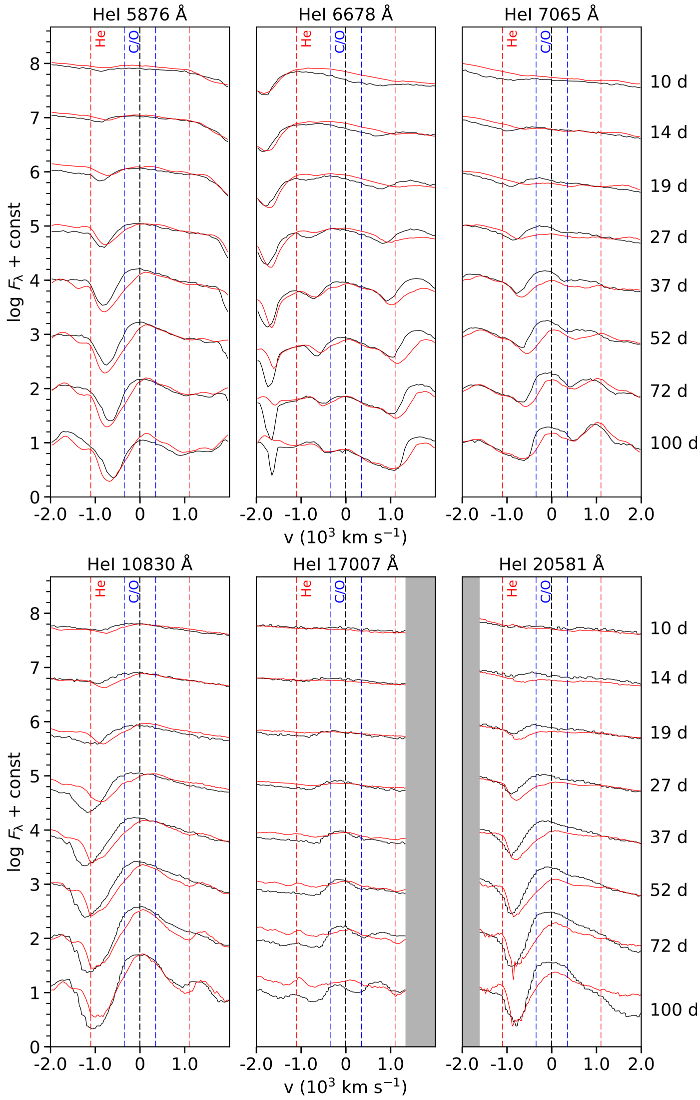

Fig. 6. Evolution of optical (upper panel) and NIR (lower panel) helium lines for the standard model (black) compared to the observations of SN 2011dh (red). Otherwise as in Fig. 5.

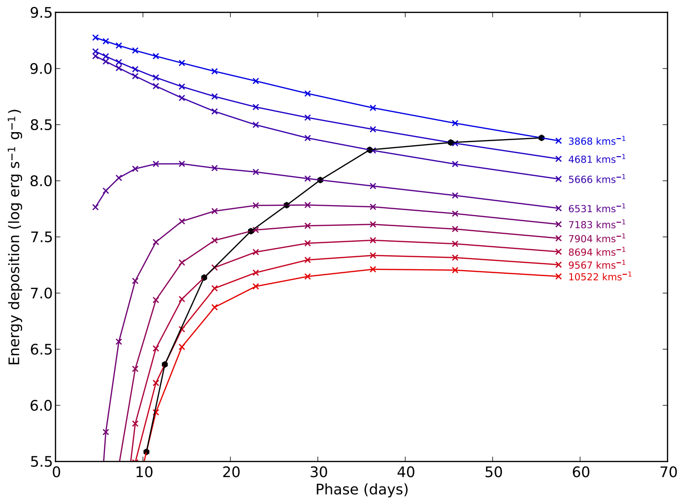

Fig. 7. Evolution of the radioactive energy deposition in the helium envelope (red to blue crosses) and the position of the (Rosseland) continuum photosphere (black circles) for the standard model.

are strong at all times, the contribution increases after ∼40 days when the core, rich in these elements becomes increasingly transparent (see Fig. 3). The upper panel of Fig. 8 shows the evolution of the Ca II 3934,3968 Å, Ca II 8498,8542,8662 Å **(hereafter Ca II triplet)** and [Ca II] 7291,7323 Å lines compared to SN 2011dh. After ∼15 days the evolution of these lines is well reproduced by the model. However, at earlier times absorption in the Ca II 3934,3968 Å **lines and the Ca II triplet** extend further out in the model. Again, this is possibly an effect of the choice of initial conditions, **where we neglect the initial cooling of the explosion energy.**

The lower panel of Fig. 8 shows the evolution of the [O I] 5577 Å, [O I] 6300,6364 Å, O I 7774 Å, O I 11290,11300 Å and Mg I 15040 Å lines compared to SN 2011dh. The overall evolution of the oxygen lines is fairly well reproduced, but the O I 5577 Å, 7774 Åand 11290,11300 Å lines appear later and are initially weaker than observed for SN 2011dh. The O I 9263 Å line is also present in the model but is blended with the [Co II] 9338,9344 Å lines (see Sect. 3.2.5).

In the model, the early (near peak) feature at ∼9200 Å is mainly caused by the Mg II 9218,9244 Å lines **(check this)**, and later the Mg I 15040 Å line appears. Similar to the oxygen lines, the Mg I 15040 Å line appears later and is initially weaker that observed for SN 2011dh. We note, that whereas the radioactive **Ni/He** material is mixed into the helium envelope in the model, the oxygen and magnesium rich material is not, which may explain the early suppression of the oxygen and magnesium lines compared to observations.

As mentioned in Sect. 3.2.2, the Na I 5890,5896 Å lines overtake He I 5876 Å line at ∼60 days, and as seen in Fig. 6 the subsequent evolution is well reproduced. In the model, the feature emerging at ∼11800 Å after ∼60 days is mainly caused by the C I 11760 Å line **(check this)**, and towards ∼150 days the [C I] 8727 Å line begins to contribute significantly to the blend with the Ca II **triplet**.

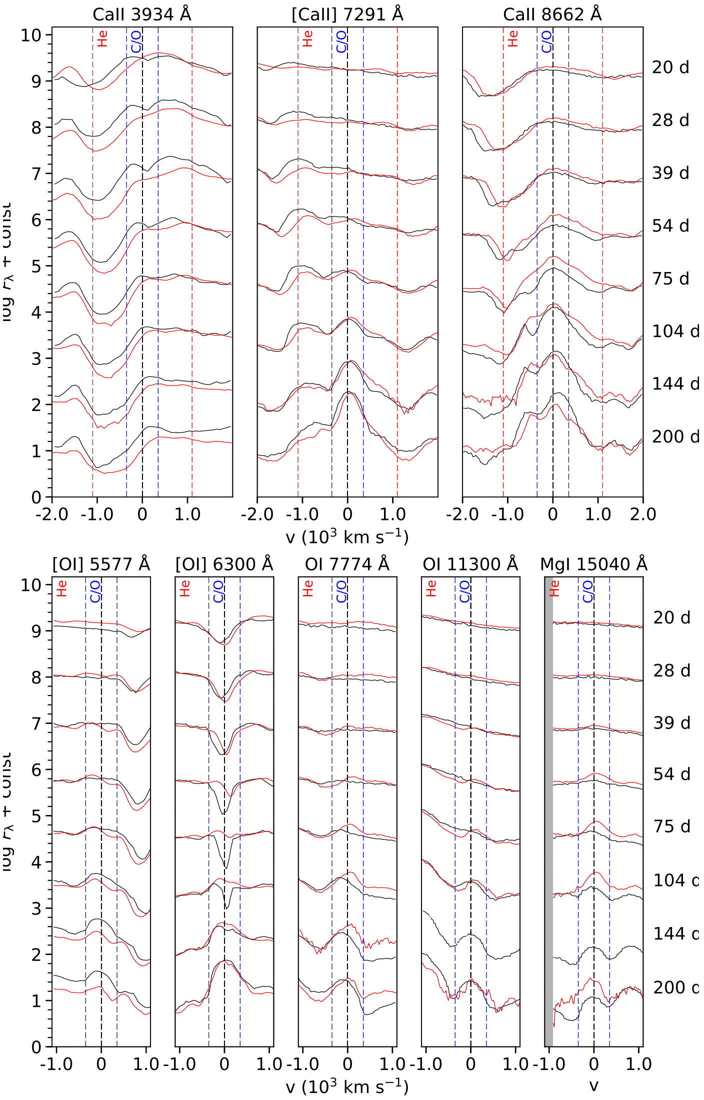

Fig. 8. Evolution of calcium, oxygen and magnesium lines for the standard model (black) compared to the observations of SN 2011dh (red). Spectra from 8 logarithmically spaced epochs between 20 and 200 days are shown.

3.2.4. Scandium to manganese

The (line) contribution from elements in the scandium to manganese range is shown in Fig. 2, and is dominating in the 3000-4000 Å region and important in the 4000-5000 Å region at all times. After ∼40 days it also contributes significantly to the optical emission redwards 5000 Å. The emission is the result of scattering and fluorescence in numerous transitions, and individual lines are hard to distinguish. Line-blocking by elements in the scandium to manganese range is important for the suppression of the emission bluewards ∼5000 Å, and in particular in the 3000-4000 Å region, corresponding roughly to the *U*-band.

3.2.5. Iron to nickel

The (line) contribution from elements in the iron to nickel range is shown in Fig. 2, and this contribution is strong at all times, in particular in the 4000-5500 Å range. After ∼40 days the contribution increases also at other wavelengths, likely due to emission from the increasingly transparent core (see Fig. 3), where about half of the **Ni/He** material resides. Except for the *U*-band (see Sect. 3.2.4), blocking through scattering and fluorescence in numerous iron lines is the main cause for the suppression of the emission bluewards ∼5500 Å, so important in shaping the spectra of stripped-envelope (SE) SNe. However, with a few exceptions, like the Fe II 5169 Å line, individual iron lines are typically strongly blended and hard to distinguish. The contribution from nickel is insignificant at all times, but after ∼50 days cobalt begins to contribute to the spectrum with several distinct lines.

Figure 9 shows the evolution of the Fe II 5169 Å and [Co II] 9338,9344 Å, [Co II] 10190,10248,10283 Å and [Co II] 15475 Å lines compared to SN 2011dh. The Fe II 5169 Å line is reasonably well reproduced, but initially absorption extends to higher velocities than observed, a discrepancy that disappears towards 150 days. The overall evolution of the cobalt lines is fairly well reproduced, but note that the [Co II] 9338,9344 Å lines are blended with the O I 9338,9344 Å lines. The iron and cobalt lines are interesting as they are directly linked to the distribution of the **Ni/He** material in the ejecta, and the width of the cobalt lines seems to suggest that this distribution is similar in SN 2011dh as in the model. However, in E15 we reached a somewhat different conclusion from analysis of the profile of the [Fe I] 7155 Å line, which appears later, and which only extends to ∼2000 km/s.

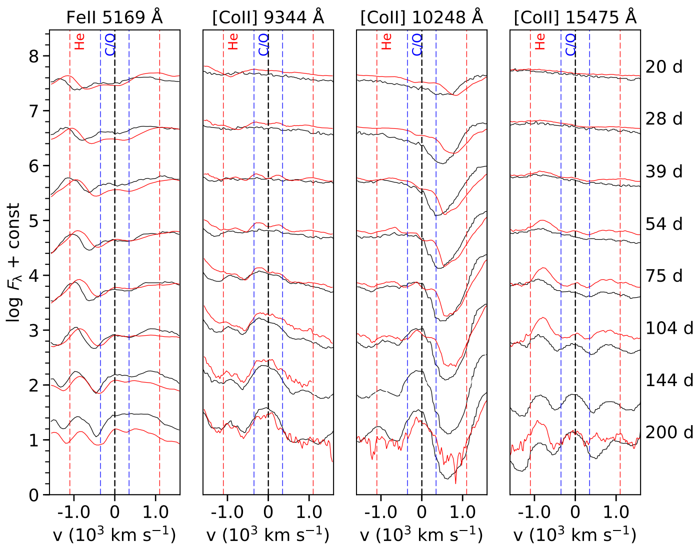

Fig. 9. Evolution of iron and cobalt lines for model the standard model (black) compared to the observations of SN 2011dh (red). Otherwise as in Fig. 8.

3.2.6. The infrared spectrum

The near-infrared and mid-infrared spectrum is of special interest because of the relatively isolated lines especially in the nebular phase. Because of their low excitation temperature these lines are also relatively insensitive to temperature and therefore especially suitable for abundance estimates. Several elements, like Ne and Ar, also have some of the few strong lines in this range. The usefulness of this range was demonstrated by the Kuiper Airborne Observatory (KAO) observations of SN 1987A and similar observations of more distant SNe will be possible with the NIRSPEC and MIRI instruments on the James Webb Space telescope (JWST). In Jerkstrand et al. (2015) the optical and near-IR were discussed, but not in the mid-IR or photospheric phase. Because of their obvious interest for JWST we will in this section discuss this in some detail.

In Fig. 10 we show the full spectra at three representative epochs. The IR spectrum at 26 days, close to maximum, is mainly an extension to the optical spectrum, with a few strong He I lines at $1.083, 2.058, 4.2959$, and 7.456 μm and a strong continuum. While the 1.083 μm line has a strong P-Cygni absorption the other lines are mainly in emission. At 100 days the IR spectrum is becoming more nebular with strong emission lines from [Ni II] 6.636 μm, [Ar II] 6.985 μm, [Co II] 10.522 μm, and [Co III] 11.883 μm.

The last spectrum at 308 days is fully nebular above $\sim$ 2.5 μm. There is at this phase only a weak continuum. In the NIR lines of [Fe II] 1.26, 1.53, 1.644 μm and 1.81 μm are strong. The line at $\sim$ 1.64 μm is, however, a blend of [Si I] 1.646 μm and [Fe II] 1.644 μm. The MIR lines have luminosities comparable to the optical lines due to the decreasing temperature. In addition to the [Ni II] 6.636 μm, [Ar II] 6.985 μm, [Co II] 10.522 μm, and [Co III] 11.883 μm, which are strong at 100 days, also [Ne II] 12.814 μm, [Fe II] $17.936, 24.519, 25.988, 35.772$ μm, [Fe III] $22.925, 33.038$ μm, [Co II] 10.522 μm, and [Co III] 11.883 μm are now strong.

Most of the lines correspond to fine-structure transitions in the ground state multiplets, which are close to be in LTE. They are therefore sensitive to the ionization fractions of the ions and elemental abundances, but less so to the temperature (as $kT/h\nu$ is usually small). **optical depths?**

3.2.7. Line velocities

Figure 11 shows the velocity evolution of the absorption minima of the Hα, Hβ, He I 5876 Å, He I 6678 Å, He I 10830 Å, He I 20581 Å, O I 7774 Å and Fe II 5169 Å lines, as well as the (Rosseland mean) continuum photosphere (compare; E15: Fig. 14). The hydrogen lines show the highest velocities, have a flat evolution, and as discussed (Sect. 3.2.1), they approach the velocity of the interface between the helium and hydrogen envelopes. The evolution is mostly in agreement with observations, but the high Hα velocities observed before ~10 days for SN 2011dh are not reproduced by the model, which could again be related to our choice of initial conditions. The helium lines appear between 10 and 15 days near the photosphere and then evolve quite differently, where the He I 10830 Å velocity increases towards that of Hα, the He I 20581 Å velocity stays almost flat, and the He I 5876 Å and 6678 Å velocities decline. The evolution of the He I 10830 Å and 20581 Å velocities is in quite good agreement with observations, whereas the He I 5876 Å and 6678 Å velocities differ more.

As discussed (Sect. 3.2.3), the O I 7774 Å line appears later than in SN 2011dh, but the velocity evolution is otherwise similar, being rather constant at ~6000 km/s. The evolution of the Fe II 5169 Å velocity follows that of the (Rosseland mean) continuum photosphere until ~30 days, confirming the common assumption (e.g. E14) that this line is a good tracer of the photosphere during the diffusion phase. However, as mentioned before, this velocity is higher than observed for SN 2011dh, although the discrepancy disappears towards 150 days (see Fig. 9). It is worth noting that the Fe II 5169 Å velocity reaches a plateau near ~6000 km s^{-1} at ~40 days, a value close to the outer border of the inner helium envelope. This is a hint that the amount of **Ni/He** material mixed into this part of the helium envelope could be too large, which in turn could force the photosphere to too high velocities. On the other hand, the width of the cobalt lines (Sect. 3.2.5) does not give support for this suspicion.

3.3. *Photometric evolution*

Figure 12 shows the broad-band lightcurves for the standard model between 0 and 150 days compared to observations of SN 2011dh. In agreement with observations, the maximum occurs at increasingly later times for redder bands and the drop onto the tail is more pronounced (deeper and faster) for bluer bands. Also in agreement with observations, the early (before 100 days) tail decline rates are generally higher for redder bands, with the *J*-band lightcurve having the steepest slope and the *U*-band lightcurve being almost flat. As has been noted in several sample studies (e.g. Taddia et al. 2015, 2018), the aforementioned behaviour of the maxima and the subsequent decline is shared not only by SN 2011dh, but by SE-SNe in general. It is also in agreement with the SE-SNe NLTE models presented by Dessart et al. (2015, 2016), and the lightcurves of the Type IIb model 3p65Ax1 are particularly similar to those of the standard model.

Although the overall agreement with observations is quite good, there are several differences between the model and the observations of SN 2011dh worth noting. Most notable are the differences in the *U*, *J* and *K*-bands and the evolution between 25 and 50 days, which is slower in *R* and bluer bands than observed for SN 2011dh. The growing **excess** in the *K*-band could be related to dust formation in the ejecta (E15), **Note, however, that there is no NIR observation between ~100 and ~200 days, so the evolution in this period is uncertain.** Some of

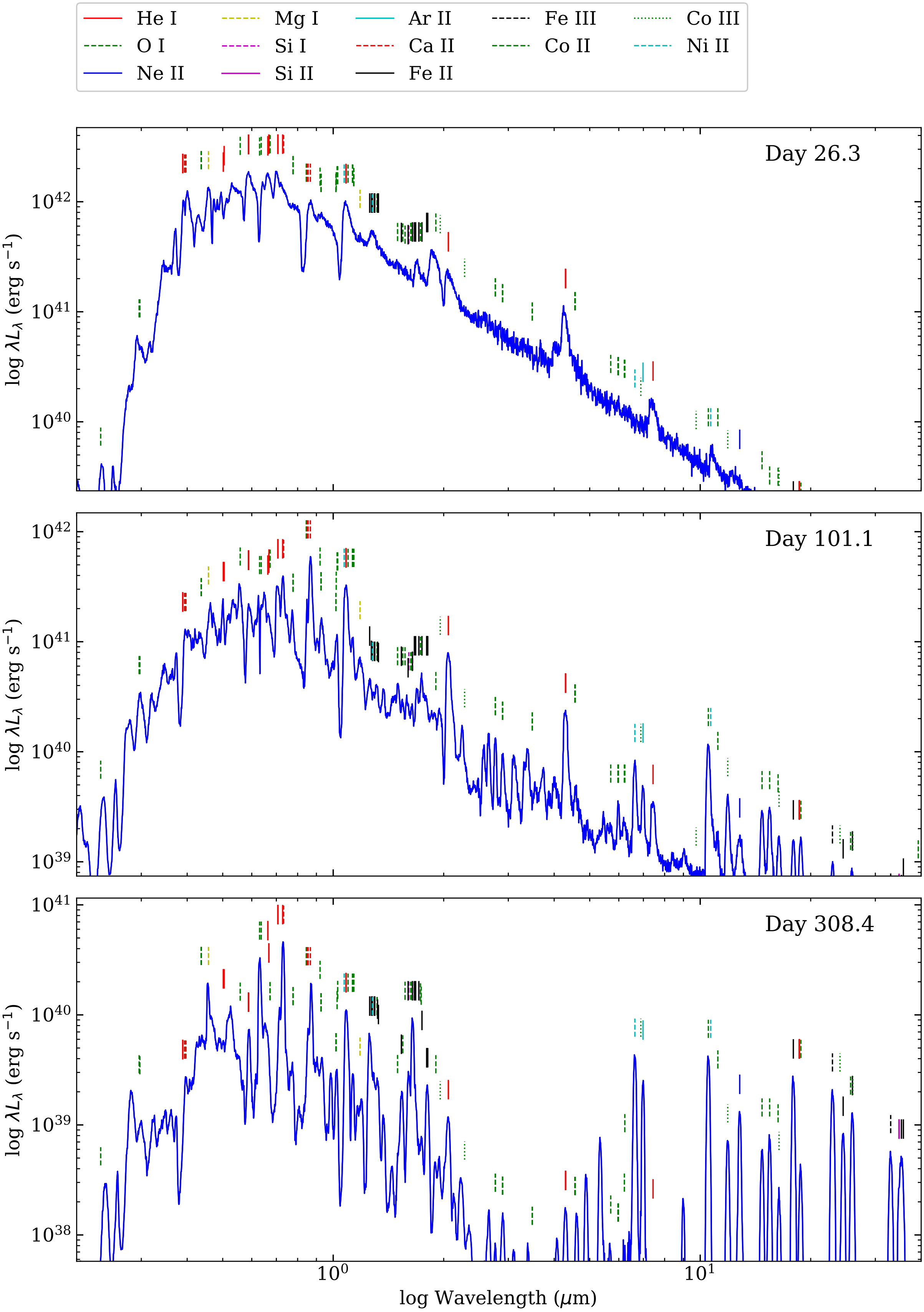

Fig. 10. Optical, NIR and MIR spectra for the standard model at 26 days (near peak), 101 days and at 308 days (nebular phase). The vertical lines shows the main contributions from the different ions in the legend above the plots.

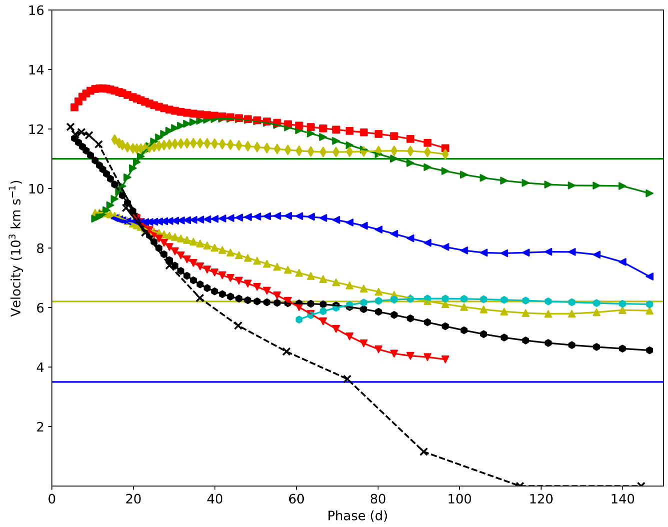

Fig. 11. Velocity evolution of the absorption minimum of the Hα (red squares), Hβ (yellow diamonds), He I 5876 Å (yellow upward triangles), He I 6678 Å (red downward triangles), He I 10830 Å (green rightward triangles), He I 20581 Å (blue leftward triangles), O I 7774 Å (cyan circles) and Fe II 5169 Å (black circles) lines for the standard model. The black crosses show the velocity evolution of the (Rosseland mean) continuum photosphere, whereas the horizontal lines mark the outer borders of the carbon-oxygen core (blue) and inner/outer (green/yellow) helium envelope.

the discrepancy in the U-band could **possibly** be explained by an underestimate of the extinction, but not all as the discrepancy is **only seen on the tail.**

3.4. Colour evolution

Figure 13 shows the intrinsic $U-V$, $B-V$, $V-I$ and $V-K$ colour evolution for the standard model between 0 and 100 days compared to observations of SN 2011dh. Initially, we see a blueward trend in all colours reaching a minimum at ∼10 days. Subsequently all colours redden and reach a maximum at ∼40 days, in turn followed by a slow blueward trend for all colours, although the $V-I$ colour stays almost constant. This behaviour is in agreement with observations, although SN 2011dh does not show an initial blueward trend in the $U-V$ and $B-V$ colours, likely due to the influence of an initial cooling tail, not present in the model due to our choice of initial conditions.

As has been noted in several sample studies (e.g. Stritzinger et al. 2018), the properties of the colour evolution discussed here are shared not only by SN 2011dh, but by SE-SNe in general. They are also in agreement with the SE-SNe NLTE models presented by Dessart et al. (2015, 2016), and the colour evolution of their Type IIb model 3p65Ax1 is particularly similar to that of our standard model. As was noted for the lightcurve, the model evolution after ∼20 days is a bit slower than observed for SN 2011dh. The model $V-I$ and $U-V$ colours are bluer than observed for SN 2011dh, reflecting differences in the I- and U-bands.

3.5. Bolometric evolution

Figure 12 shows the pseudo-bolometric UV to MIR lightcurve for the standard model between 0 and 150 days compared to observations of SN 2011dh. Similar to the comparison of the

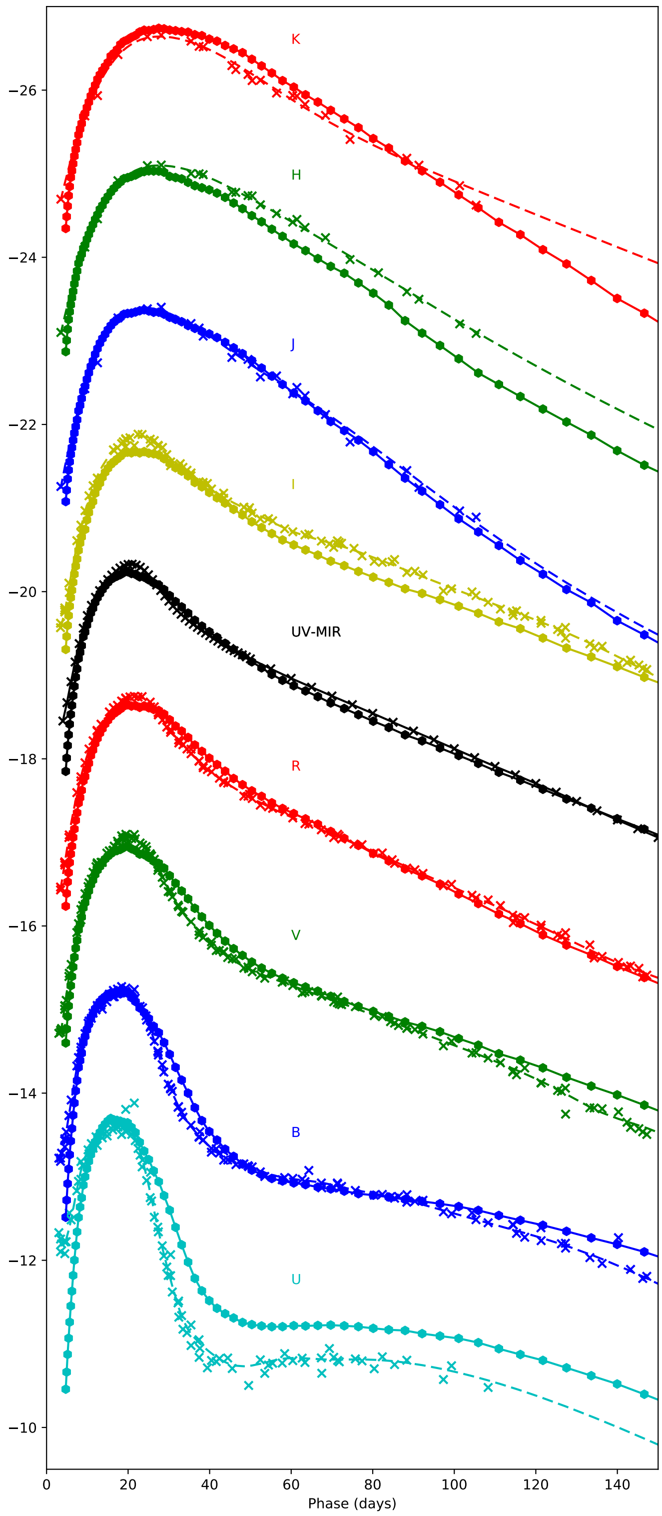

Fig. 12. Broadband and bolometric lightcurves for the standard model (solid lines and circles) compared to observations of SN 2011dh (dashed lines and crosses). From bottom to top we show the U (cyan), B (blue), V (green), R (red), UV to MIR pseudo-bolometric (black), I (yellow), J (blue), H (green) and K (red) lightcurves, which for clarity have been shifted with 2.6, 1.2, 0.0, -1.4, -3.5, -4.4, -5.8, -7.5, -8.9 mags, respectively.

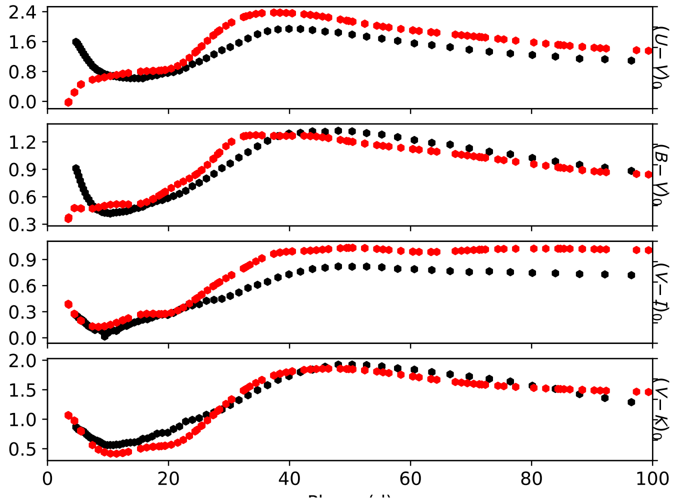

Fig. 13. $U-V$, $B-V$, $V-I$ and $V-K$ intrinsic colour evolution for the standard model (black) compared to observations of SN 2011dh (red).

broad-band lightcurves, the model bolometric lightcurve is not a perfect match and is broader than the observed one. Because the photospheric velocity is higher in the model (Sect. 3.2.7), this might indicate that a lower ejecta mass is needed. On the other hand, the mixing of the radioactive **Ni/He** material plays a stronger role when non-thermal processes are taken into account (Paper I), and there are several indications (Sects. 3.2.3, 3.2.5 and 3.2.7) that the mixing may differ from that of SN 2011dh **(Check these arguments, this discussion is currently a bit vague)**. We leave a further exploration of this, which would require a new grid of models to be constructed, for future work.

4. The effect of macroscopic mixing

Mixing of the SN ejecta occurs in the explosion due to hydrodynamical instabilities (e.g. Mueller et al. 1991), and is thought to take place on macroscopic scales only (e.g. Fryxell et al. 1991). The resulting 3-D structure is further altered by the expansion of clumps containing radioactive material due to heating from radioactive decays (e.g. Herant & Benz 1991).

In JEKYLL, the macroscopic mixing of the ejecta is simulated through use of the virtual **grid** method (J11), where the compositional layers are assumed to be fragmented into spherical clumps, and mixed with each-other. As JEKYLL is the only spectral-synthesis code that combines time-dependence, NLTE and a treatment of the macroscopic mixing, it is of great interest to investigate the effects of the macroscopic mixing on our results. To achieve this we compare the macroscopically mixed standard model presented in Sect. 3 with a microscopically mixed version, where the composition and density have been averaged over the compositional zones. To investigate the effects of the clumping geometry, we also explore a set of macroscopically mixed models differing in the expansion of the **Ni/He** and Si/S clumps as well as the sizes of the clumps. The full set of models and their differences are described in Sect. 2.5.

As we will see, the macroscopic mixing has several effects, both on the state of matter and the radiative transfer, and in the latter case a geometrical aspect enters the problem. Below we discuss the effects on the state of matter, the radiative transfer, the radioactive energy deposition, and the observed spectra and lightcurves.

4.1. State of matter

The different composition and density in the clumps compared to microscopically mixed ejecta, give rise to a different state of matter, i.e. different populations of ionized and bound states and a different temperature. This, in turn, leads to different cooling/heating rates as well as different opacities and emissivities. **In addition, the state of matter depends on the radiation field and the radioactive energy deposition, which also differs in a macroscopically mixed model.**

Figure 14 shows the temperature and electron fraction in the different clump types in the core of the macroscopically mixed standard model compared to the core of the microscopically mixed model. In the beginning of the simulation the core is handled by the diffusion solver, which assumes the temperature to be the same in all clumps. The electron fraction differs, however, due to the different composition (and density) in the clumps. At ~15 days, the core is handed over to the NLTE solver, and we see a small spread in the temperature. This indicates that the diffusion time is small but not negligible compared to the decay and expansion timescales, in agreement with what was discussed in Sect. 2.2. After ~50 days we see an increasing spread in the temperature, likely related to the different composition (and density) in the clumps. The spread in electron fraction remains large at all times, **and as expected the election fraction tends to be higher in clumps with lower ionization potential.**

The density in the clumps differs from that in microscopically mixed ejecta, but also depends on the clumping geometry, and one important effect is on the degree of ionization. This **is illustrated by** Fig. 15, which shows the electron fraction in the **Ni/He** and O/Ne/Mg clumps in the core for the macroscopically mixed models with and without expansion of the **Ni/He** and Si/S clumps. As seen in the figure, the electron fraction is higher in the **Ni/He** clumps and lower in the O/Ne/Mg clumps in the model with expanded **Ni/He** and Si/S clumps, which is expected as the density is lower in the expanded **Ni/He** clumps and higher in the compressed O/Ne/Mg clumps. A similar effect can be seen in the helium envelope, in particular for the model with strong expansion of the **Ni/He** clumps. Among other things, the degree of ionization affects the electron scattering opacity in the clumps, and we will discuss this issue more in the next section.

One important effect of the different composition in **microscopically mixed ejecta** is that strong coolants as calcium are distributed uniformly, and may overtake the cooling from other elements. This is especially important in the nebular phase, and influences lines driven by collisional cooling as the [O I] 6300,6364 Å and [Ca II] 7291,7323 Å lines. This is illustrated by Fig. 16, where we show the net collisional cooling[9] for these lines, as well as the total net collisional cooling for iron lines, in the core of the macroscopically mixed standard model and the microscopically mixed model. As seen in the figure, there is a strong difference between these models, and the net collisional cooling for the [Ca II] 7291,7323 Å line is much higher in the microscopically mixed model where calcium has been uniformly distributed. At the same time, the **net** collisional cooling for the [O I] 6300,6364 Å line is much smaller in the microscopically mixed model, whereas the iron lines are less affected.

4.2. Radiative transfer

Except for the different state of matter in the clumps, which affects the opacities and emissivities, the geometrical arrangement

[9] **Difference between collisional cooling and heating.**

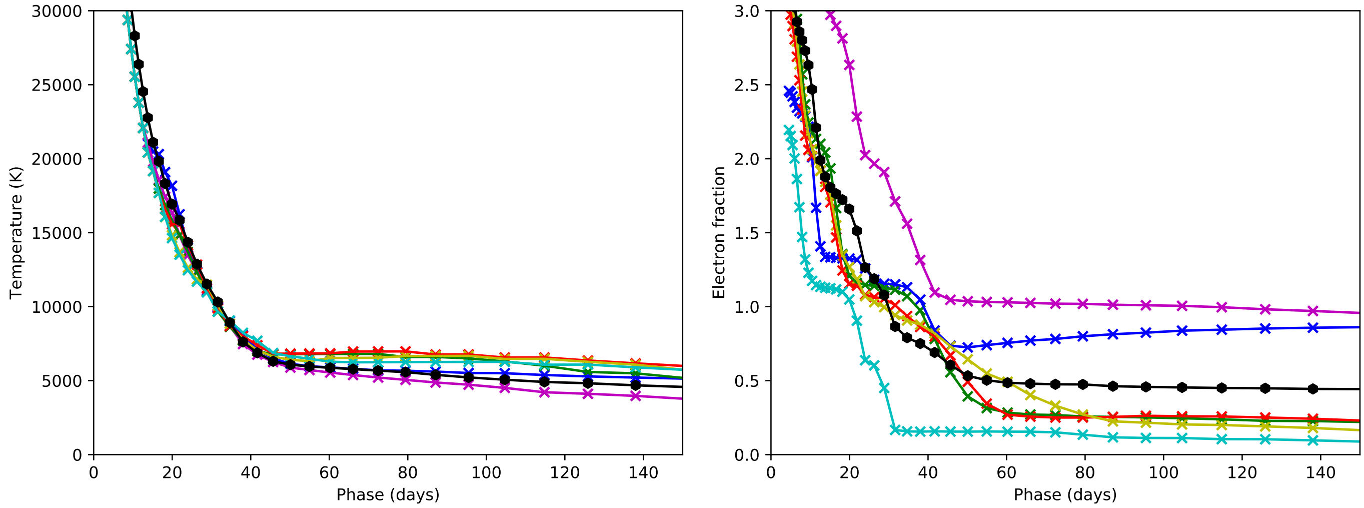

Fig. 14. Evolution of the temperature (left panel) and the electron fraction (right panel) in the **Ni/He** (blue), Si/S (magenta), O/Si/S (green), O/Ne/Mg (red), O/C (yellow) and He/C (cyan) clumps in the core of the macroscopically mixed standard model compared to the core of microscopically mixed model (black).

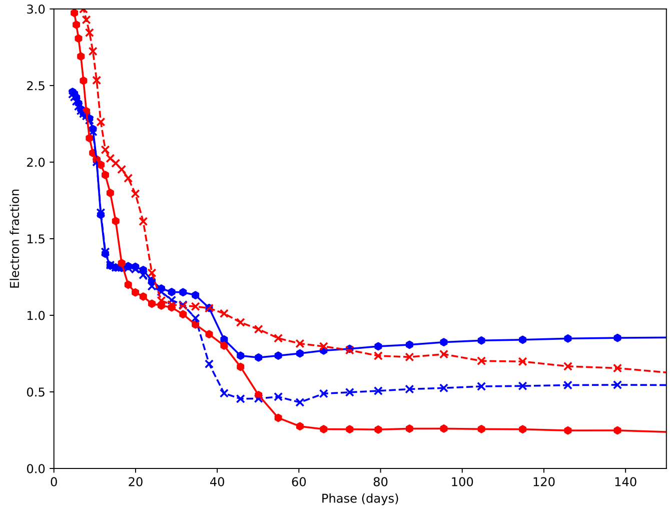

Fig. 15. Evolution of the electron fraction in the **Ni/He** (blue) and O/Ne/Mg (red) clumps in the core of the macroscopically mixed models with (circles and solid lines) and without (crosses and dashed lines) expansion of the **Ni/He** and Si/S clumps.

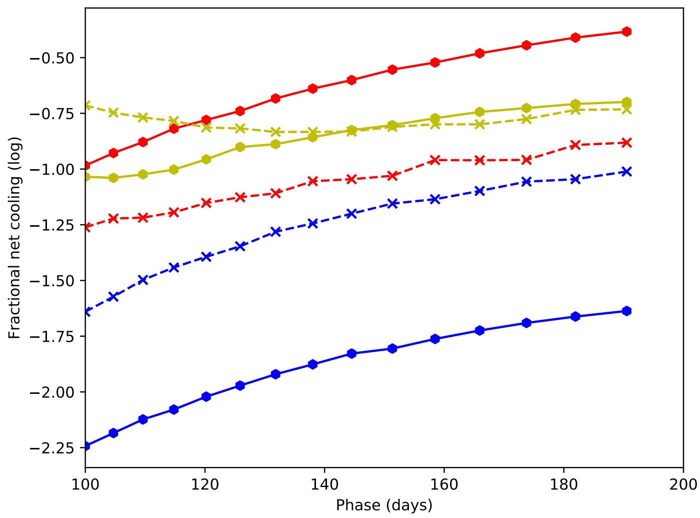

Fig. 16. Evolution of the (fractional) net collisional cooling in the nebular phase for the Fe lines (yellow) and the [O I] 6300,6364 Å (blue) and [Ca II] 7291,7323 Å (red) lines in the core for the macroscopically mixed standard model (crossed and dashed lines) compared to the microscopically mixed model (circles and solid lines).

of these also affects the radiative transfer. In particular, it affects the diffusion time, which is governed by the mean free path. In a macroscopically mixed medium that is spherically symmetric on average (which is assumed in JEKYLL), and in the limit of many clumps, the mean free path can be expressed as an effective mean free path $\hat{\lambda}_\nu(r)$, which is an average over all random arrangements of the clumps. In Appendix A we discuss the effective mean free path in more detail, and derive the diffusion approximation for such a medium in the case of a uniform[10] energy density $u_\nu(r)$ (which is assumed in the diffusion solver). This diffusion approximation differs from the ordinary one only in that the Rosseland mean opacity is replaced by an effective Rosseland mean opacity based on the effective mean free path.

As shown in Appendix A, in the case of a uniform energy density, there are a few important limiting cases in which the geometrical average of the mean free path simplify. First, in the limit of optically thin clumps, the effective opacity ($\hat{\kappa}_\nu = (\hat{\lambda}_\nu\, \rho)^{-1}$) is given by a *mass-average* of the **material** opacity in the different clump types, and is independent[11] of the **clumping** geometry (i.e. the filling factors and the sizes of the clumps). Second, in the limit of optically thick clumps, the effective mean free path is given by a *volume-average* of the mean free path in the different clump types, and depends on both the **clumping** geometry and the material opacity. Finally, in the limit of two distinct classes of clumps, one optically thick and one optically thin, the effective opacity depends *only* on the **clumping** geometry, and is independent of the material opacity. This geometrical limit is discussed further in Appendix A.

Armed with this knowledge we now turn to our models. Figure 17 shows the effective Rosseland mean optical depth in the

[10] In all clumps at a specific radius.

[11] **Except implicitly through the dependence of the material opacity on the density.**

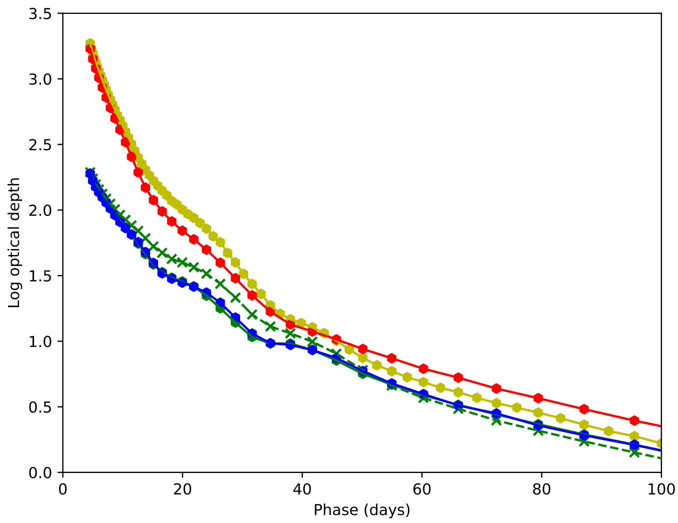

Fig. 17. Evolution of the Rosseland mean optical depth in the core for the macroscopically mixed standard model (blue circles) compared to the microscopically mixed model (red circles). In addition, we show macroscopically mixed models with no expansion of the **Ni/He** and Si/S clumps (yellow circles), and with strong expansion of the **Ni/He** clumps in the helium envelope (green circles). Finally, we show a version on the latter model where the number of clumps have been increased with 100 times (green crosses).

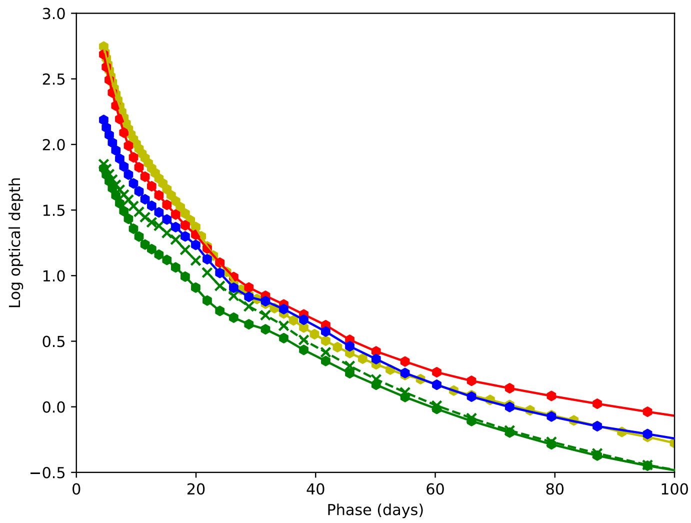

Fig. 18. Evolution of the Rosseland mean optical depth in the inner helium envelope for the macroscopically mixed standard model (blue circles) compared to the microscopically mixed model (red circles). In addition, we show macroscopically mixed models with no expansion of the **Ni/He** and Si/S clumps (yellow circles), and with additional expansion of the **Ni/He** clumps in the helium envelope (green circles). Finally, we show a version of the latter model where the number of clumps have been increased with 100 times (green crosses).

core for the full set of models. As seen in the figure, the effect of the macroscopic mixing is dramatic and mainly caused by the expansion of the clumps containing radioactive material. While the effective Rosseland mean opacity in the model without expansion of these clumps is similar to that in the microscopically mixed model, it is almost ten times lower in the standard model. This can be understood, because at early epochs the clumps are in the optically thick regime, and in this limit the effective mean free path is given by a volume average over the different clump types. In the standard model, the volume is dominated by the **Ni/He** clumps which due to expansion have a much longer mean free path. In Appendix A we show that if the opacity is uniform and unaffected by the expansion, and one type of clumps have been expanded by a factor f_E to achieve a filling factor of Φ_E, the decrease of the effective opacity in the optically thick limit is given by

$$R = \frac{(1-\Phi_E)^2}{(1-\Phi_E/f_E)} + \Phi_E\, f_E \geq 1, \tag{1}$$

which gives $R \approx 8.5$ for the standard model. If Φ_E is large, $R \approx \Phi_E\, f_E$, and if Φ_E is small, $R \approx 1 + \Phi_E\, f_E$, which shows that a considerable decrease of the effective opacity can be achieved in a wide range of cases. After ∼40 days, the clumps gradually move into the optically thin regime, and the geometrical effect on the effective Rosseland mean opacity disappears. However, as seen in the figure, the effective Rosseland mean opacity is still lower in the standard model. This can be understood, because in the optically thin limit the effective opacity is given by a mass-average over the different clump types. In the standard model, the mass is dominated by the oxygen-rich clumps, which due to compression have a lower degree of ionization (Sect. 4.1), and therefore a lower electron scattering opacity. This recombination effect, which occurs in the optically thin regime, is similar to the findings by Dessart et al. (2018), although in their work the compressed clumps were surrounded by a void medium.

It is also warranted to investigate the effect of the clumps size on the effective Rosseland mean opacity. The clumps size is important because if these are small enough we move into the optically thin regime. As seen in Fig. 17, if the number of clumps is increased by a factor of 100 (corresponding to $10^{3/2}$ times smaller clumps), the effective Rosseland mean opacity becomes considerably higher than in the standard model between ∼10 and ∼50 days. Before this, the clumps in both models are still in the optically thick regime, and after this, the clumps in both models have entered the optically thin regime.

As shown in Fig. 18, the effective Rosseland mean **optical depht** in the inner helium envelope, where the **Ni/He** clumps are mixed with helium-rich clumps, behaves similarly as in the core. Note, however, that in the standard model, where the **Ni/He** clumps have been expanded by a factor of 5, the effect on the effective Rosseland mean opacity is weaker, whereas in the model with strong (a factor of 8.5) expansion of these clumps, it is of similar magnitude as in the core.

The transition from the optically thick to the optically thin regime is illustrated by Fig. 19, where we show the effective Rosseland mean opacity in the inner helium envelope for the model with strong expansion of the **Ni/He** clumps together with the corresponding optically thick and thin limits. As seen in the figure, the effective Rosseland mean opacity initially follows the optically thick limit, begins to deviate at ∼5 days, and then gradually approaches and finally reaches the optically thin limit at ∼60 days. Note, that the difference between the optically thick and thin limit is modulated by the opacity in the clumps, which initially is higher in the helium-rich clumps due to a higher bound-free opacity, and then becomes lower due a lower electron scattering opacity. ,

In Fig. 19 we also show the effective Rosseland mean opacity for the model without expansion of the **Ni/He** and Si/S clumps. This comparison shows that the decrease of the effective Rosseland mean opacity in the model where these clumps are expanded is dominated by the geometrical effect until ∼35 days,

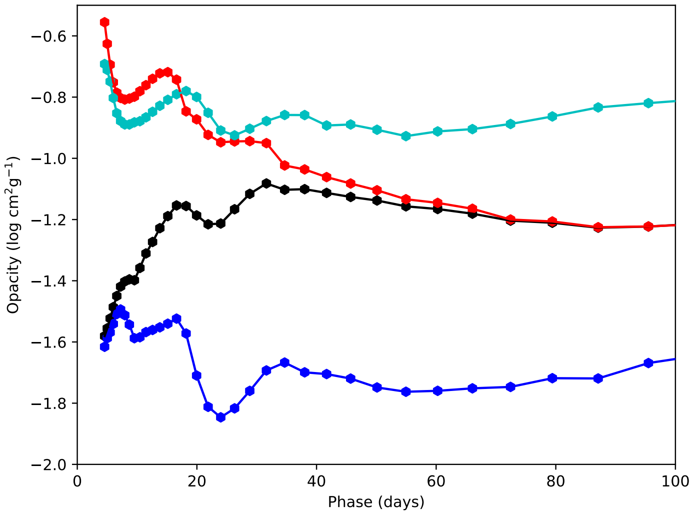

Fig. 19. Evolution of the Rosseland mean opacity in the inner helium envelope for the macroscopically mixed model with strong expansion of the Fe/He/Co clumps (black) and the corresponding Rosseland mean opacity in the limits of optically thick (blue) and thin (red) clumps. In addition, we show the evolution of the Rosseland mean opacity for the macroscopically mixed model without expansion of the Ni/He and Si/S clumps (cyan).

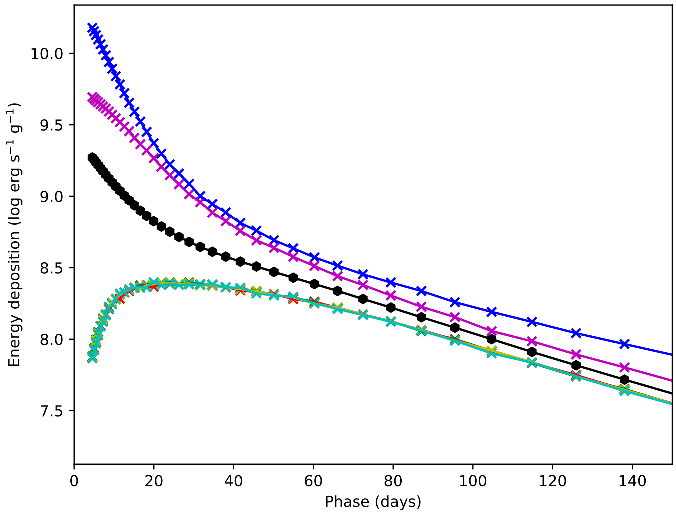

Fig. 20. Evolution of the radioactive energy deposition in the Ni/He (blue), Si/S (magenta), O/Si/S (green), O/Ne/Mg (red), O/C (yellow) and He/C (cyan) clumps in the core of the macroscopically mixed standard model compared to the core of the microscopically mixed model (black).

after which it is dominated by the decrease in material opacity in the helium-rich clumps due to the lower electron scattering opacity. These effects are complementary, and broadly speaking, the geometrical effect operates in the optically thick regime, whereas the recombination effect operates in the optically thin regime. The geometrical effect is, however, potentially much stronger.

4.3. Radioactive energy deposition

In a macroscopically mixed model the radioactive decays occur solely in the Ni/He and Si/S clumps. The leptons emitted in the decays are assumed to deposit their energy locally, whereas the deposition of γ-ray energy depends on the radiative transfer. Early on, the Ni/He and Si/S clumps are optically thick to the γ-rays and all the radioactive decay energy is deposited locally. When the Ni/He and Si/S clumps approach the optically thin regime, the γ-rays begin to leak out and may deposit their energy in other clumps. As discussed in Sect. 4.2, the radiative transfer in a macroscopically mixed model depends on the **clumping geometry**, but once the optical depth of all clumps approaches zero, this dependence is lost and the radiative transfer is governed by the mass-averaged γ-ray opacity, which is the same as in a microscopically mixed model.

Figure 20 shows the energy deposition in the different clump types in the core for the macroscopically mixed standard model compared to the microscopically mixed model. As expected, we see that the radioactive decay energy is almost solely deposited in the Ni/He and Si/S clumps at early times. At ~10 days, the γ-rays begin to leak out from the Ni/He and Si/S clumps and the energy deposition rises drastically in the other clumps. As time goes the γ-ray energy deposition in the clumps approaches a common value. However, as the leptons still deposit their energy locally in the Ni/He and Si/S clumps, the total radioactive energy deposition is allways higher in these. This difference increases with time as an increasing fraction of the γ-rays escape from the ejecta.

4.4. Observed spectra and lightcurves

We now turn to the observed lightcurves and spectra, and analyse what effect the macroscopic mixing have on these. We begin with the bolometric lightcurve, which is mainly affected by the effects on the radiative transfer discussed in Sect. 4.2, and then turn to the spectra, which are mainly affected by the effects on the state of matter discussed in Sect. 4.1.

4.4.1. Bolometric lightcurves

Figure 21 shows the bolometric lightcurves for the full set of models. Compared to the microscopically mixed model, the peak of the bolometric lightcurve is brighter, occurs earlier and is considerably narrower in the macroscopically mixed standard model, which is what we would expect from the lower effective Rosseland mean opacity in this model. Once on the tail, the difference disappears as the opacity difference decreases and the luminosity is not determined by the diffusion time anymore.

The bolometric lightcurve for the macroscopically mixed model *without* expansion of the Ni/He and Si/S clumps, which has similar effective Rosseland mean opacity as the microscopically mixed model (Sect. 4.2), is almost identical to that of the microscopically mixed model. Clearly, the expansion of the Ni/He and Si/S clumps may have a strong effect on the bolometric lightcurve through its influence on the effective Rosseland mean opacity. For the macroscopically mixed model with strong expansion of the Ni/He clumps in the helium envelope the effect is quite dramatic, and the peak occurs almost 8 days before that of the microscopically mixed model and is much brighter.

However, the effect also depends on the size of the clumps, and the bolometric lightcurve for same model with 100 times more clumps (which are therefore $10^{3/2}$ times smaller) is more similar to that of the macroscopically mixed standard model. As discussed in Sect. 4.2, the reason for this is that the geometrical effect on the effective Rosseland mean opcacity disappears when the clumps becomes optically thin. Unfortunately, no strong constraints exist on the size of the clumps and the expansion of the Ni/He and Si/S clumps (?) in the helium envelope, neither observational nor theoretical, and further work on this issue is highly warranted.

The effect of macroscopic mixing on the lightcurves is not restricted to the case explored here, and will affect the lightcurves of stripped-envelope SNe in general. It may be stronger or weaker, depending on the expansion of the clumps containg radioactive material, the amount and distribution of such material, and the size of these and other clumps. However, if the clumps containing radioactive material are expanded by a large factor to fill a large fraction of the volume, it is potentially dramatic (Sect. 4.2), as is exemplified by the case explored here. The effect could lead to systematic underestimates of the ejecta masses of stripped-envelope SNe, as it is not included in codes commonly used to estimate these from the bolometric lightcurve. We note, however, that these codes does not include NLTE either, which at least for the Type IIb model explored here works in the opposite direction (Paper I).

Recently, Dessart & Audit (2019) found a similar effect on the lightcurves Type II SNe using multi-D simulations with a simplified treatment of the matter. In these simulations, the ejecta were assumed to consist of high density clumps surrounded by a lower density medium, but the density contrast was not directly linked to the expansion of radioactive material as in our models. The authors also introduce the concept of optically tick "macroclumps", and their qualitative discussion of **the** effect on the radiative transfer is in line with our discussion of the effective opacity in the limit of optically thick clumps. We note, however, that the concept of effective opacity presented here (Sect. 4.2 and Appendix A) is quite fruitful, as it allows us to quantify the effect of the macroscopic mixing on the radiative transfer. The MC method used in JEKYLL to calculate it may be incorporated also in tradiational non-MC codes, e.g. in diffusion-based hydrodynamical codes, commonly used to calculate the bolometric lightcurves of SNe.

4.4.2. Spectral evolution

Figure 22 shows the optical spectral evolution for the macroscopically mixed standard model compared to the microscopically mixed model. Because several of the stronger features, like the ∼ 6300Å and the ∼ 8600 Å 'lines' are blends of several lines, we show in Fig. 24 the luminosities of some of the most important lines contributing to these. We first note that before the nebular phase, starting at ∼ 150 days, especially the ∼ 6300 Å feature is a complicated blend of several lines, in particular several Fe II and He I lines, while the [O I] 6300, 6364 Å lines are weak.

Initially the spectral evolution is very similar in the two models, but after ∼40 days they become increasingly different. In particular, the Ca II **triplet** and **the** [Ca II] 7291,7323 Å lines are much stronger, whereas the [O I] 6300,6364 Å lines are much weaker in the microscopically mixed model (Fig. 24). These lines are mainly driven by collisional cooling, and as discussed in Sect. 4.1, the net collisional cooling rates of the calcium lines are increased in the microscopically mixed model, whereas the net collisional cooling rate of the [O I] 6300,6364 Å lines is decreased.

As was previously pointed out by Fransson & Chevalier (1989), this is because calcium is a very effective coolant by a factor of $\sim 10^3$, and when calcium-rich material is mixed with other compositional zones it overtakes the cooling from other less efficient coolants. The difference in the [Ca II] 7291,7323 Å and [O I] 6300,6364 Å lines become very strong after ∼100 days, and it is clear that macroscopic mixing needs to be taken into account in the nebular phase for the model to be realistic. This is particularly true for the [O I] 6300,6364 Å lines, given their importance for constraining the initial mass of the progenitor star (see e.g. Jerkstrand et al. 2015).

Figure 23 shows the optical spectral evolution for the macroscopically mixed standard model compared to the model without expansion of the **Ni/He** and Si/S clumps. Initially, the spectral evolution is fairly similar, but after ∼50 days a clear difference emerges in the Ca II **triplet.** The strongest difference is seen after ∼80 days, where the line is much weaker in the model without expansion of the **Ni/He** and Si/S clumps. The difference can be traced back to emission from the Si/S clumps in the core and the degree of ionization in these clumps **(verify this)**, which is higher in the model with expanded Si/S clumps. As the Ca II **triplet** observed in SN 2011dh **is** in good agreement with that in the standard model, this suggests that the expansion of the Si/S clumps in the core is considerable in SN 2011dh. This is in line with the findings in E15 based on small-scale variations in the [O I] 6300,6364 and Mg I] 4571 Å line profiles, which suggest that the compression of the oxygen-rich clumps in the core is also considerable.

Further and more robust constraints on the expansion/compression of the clumps can be obtained from IR observations. In Fig. 25 we show the full spectrum at 308 days for the same models as in Fig. 23. The most important difference is a change of ionization, as can be seen for especially the Mg I], Ca II, He I, [Ne II] and [Fe III] lines. As seen in the figure, several [Fe III] and [Co III] lines, which originate from the **Ni/He** clumps in the core, show strong differences between the models with and without expansion of these clumps. There are also [Fe II] and [Co II] lines available, so the (weak) temperature dependence in the [Fe III] and [Co III] line-strengths can be removed by using line-ratios between **singly and double ionized** lines. In addition, the models differ strongly in the [Ne II] 12.8 μm line, originating from the O/Ne/Mg clumps in the core **(verify this)**, as these clumps are compressed in the models with expanded **Ni/He** and Si/S clumps. In order to better constrain the expansion of the **Ni/He** clumps (as well as the compression of the O/Ne/Mg clumps), MIR observations of Type IIb SNe would therefore be very useful, something that may be possible with the JWST.

5. Conclusions

We use the new spectral synthesis code JEKYLL (Paper I) to evolve a macroscopically mixed Type IIb model through the photospheric and nebular phase. The model belongs to a set of models presented in J15, and was shown to compare well with nebular observations of SN 2011dh in J15 and E15. Here we show that **(a slightly modified version of?)** this model also reproduces the photospheric spectra and broadband lightcurves well. Some quantitative differences exist, however, and to find a model that improves the agreement is a challenge to be addressed in future work. **In particular, a better understanding of the mixing is needed.** Nevertheless, most important observational aspects of SN 2011dh, many of which are observed in other Type IIb SNe as well, are well reproduced by the model. This demonstrates that our understanding of Type IIb SNe has reached a rather mature level, and that NLTE modelling of such SNe is capable of producing realistic spectra and lightcurves, both in the photopsheric and nebular phase. We also show for the first time detailed mid-IR spectra of a Type IIb SN, demonstrating their rich content of information in especially the nebular phase.

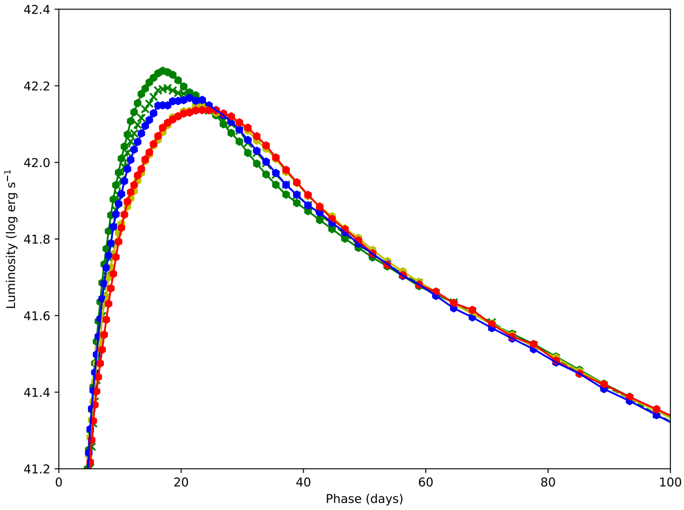

Fig. 21. Bolometric lightcurve for the macroscopically mixed standard model (blue circles) compared to the microscopically mixed model (red circles). In addition, we show macroscopically mixed models with no expansion of the Ni/He and Si/S clumps (yellow circles), and with strong expansion of the Ni/He clumps in the helium envelope (green circles). Finally, we show a version of the latter model where the number of clumps have been increased by a factor of 100 (green crosses).

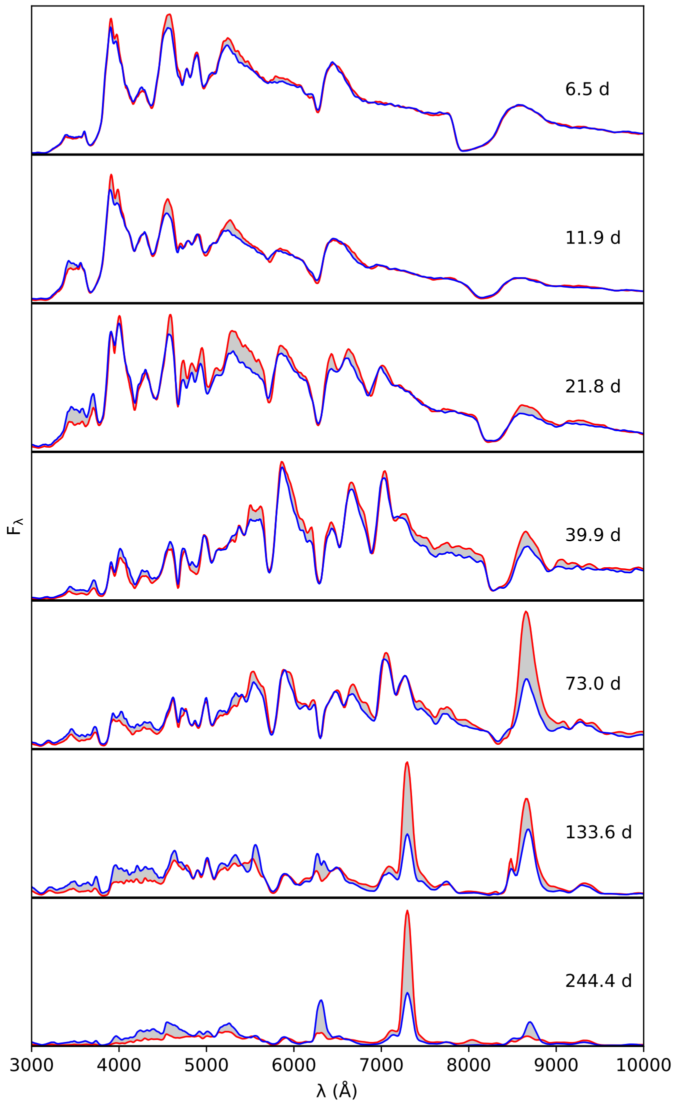

Fig. 22. Optical spectral evolution for the macroscopically mixed standard model (blue) compared to the microscopically mixed model (red), where the difference has been highlighted in grey.

We also investigate the effects of the macroscopic mixing by comparing macroscopically and microscopically mixed models, and by varying the clumping geometry in the macroscopically mixed models. In our treatment the clumping geometry is parametrized by the size of the clumps and their filling factors, where the latter are determined by the expansion of the Ni/He and Si/S clumps. In the nebular phase, we find strong effects on the collisional cooling rates in the macroscopically mixed regions, which affect the strength of lines driven by collisional cooling. For example, the [Ca II] 7291,7323 Å lines are much weaker and the [O I] 6300,6364 Å lines much stronger in the macroscopically mixed case. The reason for this is that calcium, which is a very efficient coolant, overtakes the cooling from oxygen when the calcium- and oxygen-rich clumps are mixed together.

Early on, we find strong effects on the effective Rosseland mean opacity in the macroscopically mixed regions, which in turn affects the observed lightcurves. The diffusion peak of the bolometric lightcurve is considerably narrower in the macroscopically mixed case, and differs strongly if the Ni/He clumps in the helium envelope are assumed to expand more than in our standard model. The effect is mainly geometrical, and is driven by the expansion of clumps containing radioactive material, which creates a density contrast between these clumps and the rest of the ejecta. As we show, in the case of a uniform radiation field **(clarify?)**, this always **(?)** tends to decrease the effective opacity if the clumps are optically thick. In this limit, the decrease is roughly given by the product of the filling factor and the expansion factor for the clumps containing radioactive material. The effect also depends on the typical clumps size, as it disappears when the clumps becomes optically thin. In addition to the geometrical effect, there is also a recombination effect, that tends to decrease the effective opacity in the limit of optically thin clumps, and which has been discussed by Dessart et al. (2018). These effects are complementary and operate in different regimes, but the geometrical effect is potentially stronger, and in our models it dominates.

The demonstrated effect of macroscopic mixing on the effective opacity has implications for lightcurve modelling of Type IIb SNe, as well as stripped-envelope SNe in general, and will tend to increase the estimated ejecta masses. It is therefore important to better constrain the expansion of the Ni/He clumps and the typical size of these and other clumps. Constraints on the expansion/compression of the clumps can be obtained from spectra, and observations of the Ca II **triplet** suggests that the expansion of the Si/S clumps is considerable in SN 2011dh. More robust constraints on the expansion of the Fe/He/Co clumps can be derived from observations of fine-structure lines in the MIR, as may be possible with the JWST.

As was shown in Paper I, a full NLTE solution is required to reproduce the lightcurves and spectra of Type IIb SNe, and based on the findings in this work it is clear that *both* NLTE and macroscopic mixing are essential ingredients to reproduce the lightcurves and spectra of Type IIb SNe throughout their evolution.

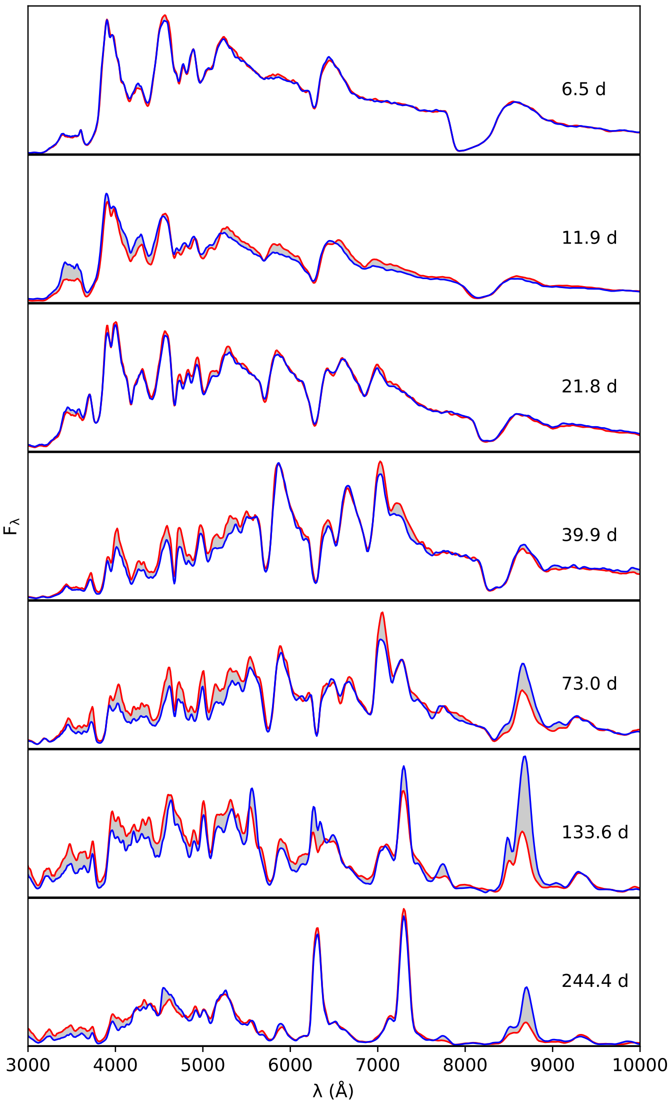

Fig. 23. Optical spectral evolution for the macroscopically mixed standard model (blue) compared to the model without expansion of the Fe/C/He and Si/S clumps (red), where the difference has been highlighted in grey.

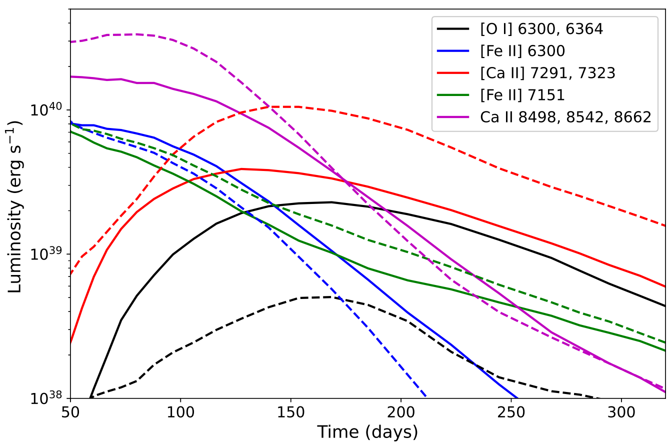

Fig. 24. Luminosities of the lines contributing to the features at ∼ 6300, 7300 and 8600Å features in the macroscopically (solid lines) and microscopically (dashed lines) mixed cases.

Appendix A: Radiative diffusion in a macroscopically mixed medium

This section needs a rewrite based on a more appropriate radiative transfer approach, a better description of the assumptions made, and probably a test against a full MC calculation. However, the results will likely hold.

Radiative diffusion in a macroscopically mixed medium differs from that in a smooth medium due to the varying mean free path in the clumps. To understand and investigate the difference we begin by re-deriving the diffusion approximation for a smooth medium. Consider the energy transported through an area dA in time dt by photons with frequency ν originating from a distance l with energy density u_ν, propagating with polar direction θ and with a path-length distribution function[12] f_ν. Using a Taylor expansion of u_ν this gives

$$dE_\nu = \frac{c}{2}\int_0^\pi \int_0^\infty f_\nu(l)\, u_\nu(r - l\cos\theta)\cos\theta\sin\theta\, dl\, d\theta\, dA\, dt \approx -\frac{c}{2}\int_0^\pi \int_0^\infty f_\nu(l)\frac{du_\nu}{dr}\, l\cos^2\theta\sin\theta\, dl\, d\theta\, dA\, dt = -\frac{\lambda_\nu c}{3}\frac{du_\nu}{dr}\, dA\, dt, \quad (A.1)$$

where λ_ν is the mean free path given by $\int_0^\infty f_\nu(l)\, l\, dl$. The flux is defined as $dE_\nu = F_\nu\, dA\, dt$ and integrating over frequency we get the general form of the diffusion approximation

$$F = -\frac{c}{3}\int_0^\infty \lambda_\nu \frac{du_\nu}{dr} d\nu \quad (A.2)$$

Assuming a blackbody radiation field this can be written as

$$F = -\frac{4acT^3}{3\kappa_R\rho}\frac{dT}{dr}, \quad (A.3)$$

where

$$\kappa_R = \int \frac{dB_\nu}{dT} d\nu \Big/ \int \lambda_\nu \frac{dB_\nu}{dT} d\nu \quad (A.4)$$

is the Rosseland mean opacity.

Consider a macrscopically mixed medium consisting of n types of randomly distributed clumps with energy density $u_{\nu,i}$ and filling factor Φ_i. In the limit of many clumps, dE_ν can be expressed as an average over all random arrangements of the clumps, and to calculate it we need to sum the contributions from photons originating from each type of clumps using an effective path-length distribution function $\langle f_{\nu,i}\rangle$, which is an average over all random arrangements of the clumps. In the following, we restrict ourselves to the case of a uniform energy density $u_\nu(r)$, which is what is assumed in the diffusion solver used in JEKYLL. In analogy with Eq. A.1 we the get

$$dE_\nu = \frac{c}{2}\sum\int_0^\pi \int_0^\infty \langle f_{\nu,i}\rangle\, u_\nu(r - l\cos\theta)\,\Phi_i\cos\theta\sin\theta\, dl\, d\theta\, dA\, dt \approx -\frac{\hat{\lambda}_\nu c}{3}\frac{du_\nu}{dr}\, dA\, dt, \quad (A.5)$$

[12] Throughout this appendix, the term distribution function refers to the probability density function.

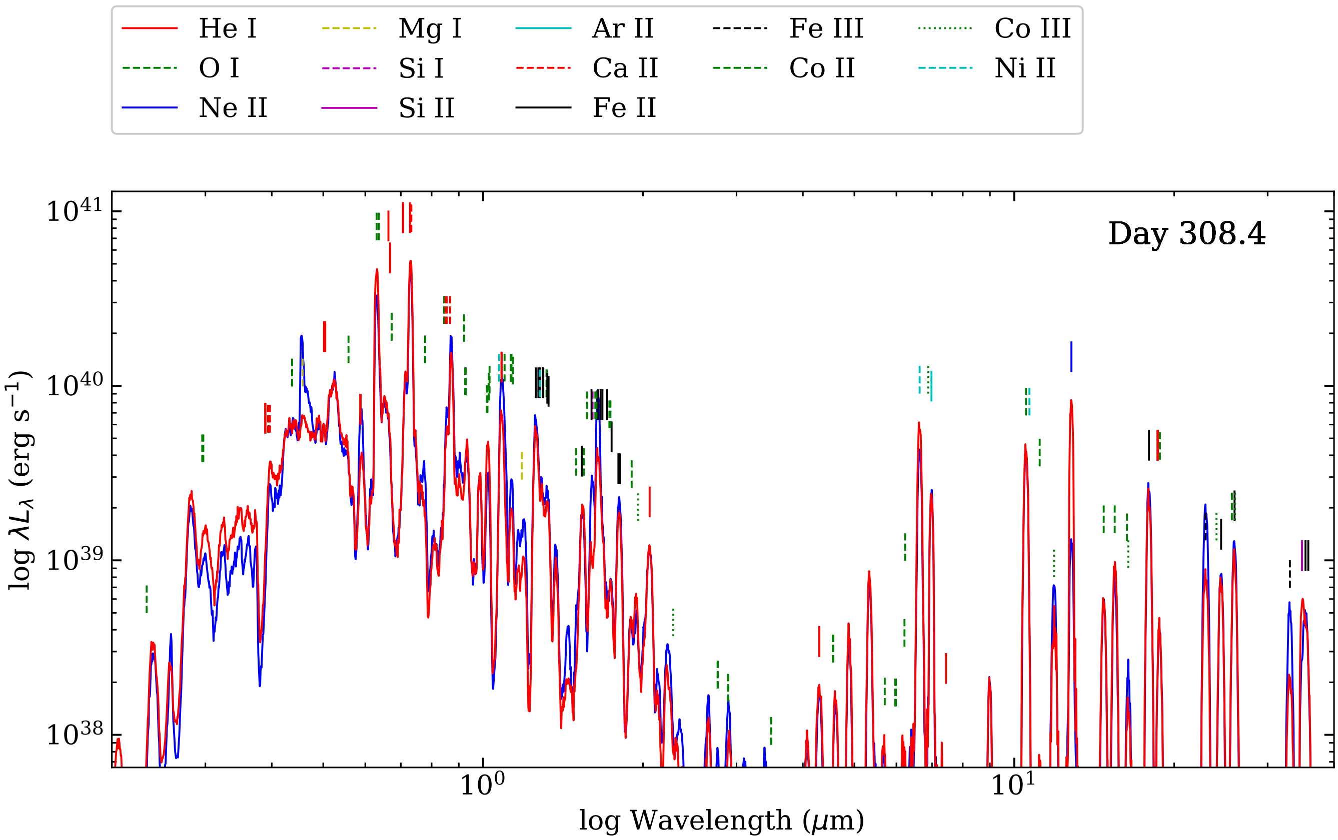

Fig. 25. Optical, NIR and MIR spectrum at 308 days (nebular phase) for the macroscopically mixed standard model (blue) compared to the model without expansion of the Fe/C/He and Si/S clumps (red).

where $\hat{\lambda}_\nu$ is the effective mean free path given by

$$\hat{\lambda}_\nu = \sum \Phi_i \, \hat{\lambda}_{\nu,i} = \sum \Phi_i \int_0^\infty \langle f_{\nu,i} \rangle \, l \, dl \tag{A.6}$$

It is also convenient to define a corresponding effective opacity as $\hat{\kappa}_\nu = (\hat{\lambda}_\nu \, \rho)^{-1}$. In analogy with Eq. A.2 we then get the general form of the diffusion approximation in a macroscopically mixed medium

$$F = -\frac{c}{3} \int_0^\infty \hat{\lambda}_\nu \frac{du_\nu}{dr} d\nu \tag{A.7}$$

Assuming a blackbody radiation field this can be written as

$$F = -\frac{4acT^3}{3\hat{\kappa}_R \rho} \, \frac{dT}{dr}, \tag{A.8}$$

where

$$\hat{\kappa}_R = \int \frac{dB_\nu}{dT} d\nu \Big/ \int \hat{\lambda}_\nu \frac{dB_\nu}{dT} d\nu \tag{A.9}$$

is the effective Rosseland mean opacity in a macroscopically mixed medium.

To calculate $\hat{\kappa}_R$ we need $\hat{\lambda}_\nu$ which in turn depends on $\langle f_{\nu,i} \rangle$. These geometrical averages of the path-length distribution functions can be written

$$\langle f_{\nu,i}(l) \rangle = \langle \exp(-\kappa_{\nu,i} \, \rho_i \, l_i) \prod_{j=0}^{n} \exp(-\kappa_{\nu,j} \, \rho_j \, l_j) \rangle =$$
$$\int \cdots \int \exp(-\kappa_{\nu,i} \, \rho_i \, l_i) \prod_{j=0}^{n} \exp(-\kappa_{\nu,j} \, \rho_j \, l_j) \; f \; dl_i \, dl_0 \ldots dl_n, \tag{A.10}$$

where i and j are the types of the originating and subsequent clumps, l_i and l_j are the (total) pathlengths through them, and $f(l_i, l_0, \ldots, l_n, l)$ the corresponding distribution function at distance l. In general, calculating them is complicated, and in JEKYLL we use a MC method, which is the same as used in the ordinary radiative transfer, except that the MC packets are terminated once an interaction with the matter is drawn.

There are a few limits, in which case the geometrical averages can be simplified. In the optically thin limit, the first exponential factor in Eq. A.10 approaches one, the number of clumps traversed before absorption approaches infinity, and the (total) pathlength distribution function approaches a delta function at the average (total) pathlengths **(not correct, clarify)**. As the probability for a point to lie within a clump of type j is just the filling factor, the average total path-length is $\Phi_j \, l$, and we get

$$\langle f_{\nu,i}(l) \rangle \approx \prod_{j=0}^{n} \exp(-\Phi_j \, \kappa_{\nu,j} \, \rho_j \, l) = \exp(-\sum_{j=0}^{n} \Phi_j \, \kappa_{\nu,j} \, \rho_j \, l) =$$
$$\exp(-\overline{\kappa_\nu} \, \rho \, l), \tag{A.11}$$

where $\overline{\kappa_\nu}$ is a mass average of the opacity over the different clump types. Therefore, in this limit, the effective mean free path is given by

$$\hat{\lambda}_\nu = \frac{1}{\rho \, \overline{\kappa_\nu}} \tag{A.12}$$

In the optically thick limit, all photons are absorbed in the originating clump, and we get

$$\langle f_{\nu,i}(l)\rangle \approx \exp(-\kappa_{\nu,i}\,\rho\, l) \tag{A.13}$$

Therefore, in this limit the effective mean free path is given by

$$\hat{\lambda}_\nu = \sum \Phi_i\, \lambda_{\nu,i}, \tag{A.14}$$

which is a volume average of the mean free path over the different clump types.

Using Eqs. A.12 and A.14, the ratio between the effective mean free path in the optically thick and thin limit (or equivalently, the ratio between the effective opacity in the optically thin and thick limit) can be expressed as

$$R_\nu = \sum \Phi_i \lambda_{\nu,i} \sum \Phi_j \frac{1}{\lambda_{\nu,j}} = \sum\sum \Phi_i \Phi_j \frac{\lambda_{\nu,i}}{\lambda_{\nu,j}} \geq 1, \tag{A.15}$$

where the last condition follows from the fact that $\lambda_{\nu,i}/\lambda_{\nu,j} + \lambda_{\nu,j}/\lambda_{\nu,i} \geq 2$. Therefore, the effective mean free path is the same in both limits only if the mean free path is the same in all clump types, and is otherwise longer in the optically thick limit. Note, that for medium with equal opacity in all clumps, Eq. A.15 can be expressed as

$$R_\nu = \sum\sum \Phi_i \Phi_j \frac{\rho_i}{\rho_j} \geq 1 \tag{A.16}$$

Therefore, in this case, the effective mean free path is the same in both limits only if the density is the same for all clump types, and is otherwise longer in the optically thick limit. In other words, the effective mean free path is increased and the effective opacity decreased by density variations.

A third limiting case is when one class of clumps are in the optically thick regime and another class of clumps are in the optically thin regime. When the optical depth approaches infinity in the optically thick clumps and zero in the optically thin clumps, the exponential factors in Eq. A.10 becomes either one or zero. In particular, the product of the exponential factors corresponding to optically thick clumps is only non-zero when the total path-length through those equals zero. As can be understood, if the path begin in an optically thin clump, the integral then corresponds to the distribution function of *not* hitting an optically thick clump at distance l. In anology with the material opacity, we then get

$$\langle f_{\nu,i}(l)\rangle = \exp(-\kappa_G\,\rho\, l), \tag{A.17}$$

where $\kappa_G\,\rho$ is the geometrical cross-section per volume produced by the optically thick clumps and κ_G the corresponding geometrical opacity. If the path begins in a optically thick clump, $\langle f_{\nu,i}(l)\rangle$ becomes a delta function a zero pathlength, and does not contribute to the effective mean free path. Therefore, we get

$$\hat{\lambda}_\nu = \sum \Phi_i/(\kappa_G\,\rho), \tag{A.18}$$

where i corresponds to the optically thin clumps.

Note, however, that the derivation above assumes that $l \gg \langle l_i\rangle$, as the photons can not hit an optically thick clump until they have escaped the originating optically thin clump. In other words, it requires that the geometrical mean free path is much larger than the size of the optically thin clumps. If the geometrical mean free path is much smaller than the size of the optically thin clumps, the effective mean free path is instead determined by the size of the optically thin clumps, and is given by

$$\hat{\lambda}_\nu = \sum \Phi_i\, \langle l_i\rangle, \tag{A.19}$$

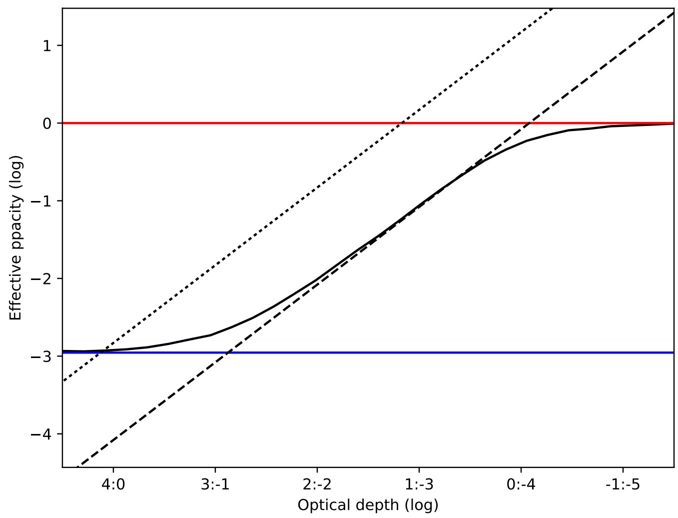

Fig. A.1. Effective opacity (black) for a homologously expanding clump-like medium with high and low density clumps of equal size and opacity, where the high density clumps have a filling factor of 0.1. We also show the optically thin (blue), optically thick (red) and geometrical clump (dashed black) and bubble (dotted black) limits. The opacity is given in arbitrary units, and the optical depth as H:L, where H and L are the optical depths in the high and low density clumps, respectively.

where i corresponds to the optically thin clumps. The geometrical limit therefore splits in two, one which we refer to as the clump limit, where $l_G \gg \langle l_i\rangle$ and the effective mean free path is given Eq. A.18, and one which we refer to as the bubble limit, where $l_G \ll \langle l_i\rangle$ and the effective mean free path is given by Eq. A.19. Following this we classify macroscopically mixed media with a high optical depth difference between the clumps as clump-like or bubble-like, depending on if the geometrical mean free path is smaller or larger than the average size of the low-optical-depth clumps.

The limits discussed are illustrated by Figs. A.1 and A.2, where we show the effective opacity for homologously expanding clump and bubble-like media consisting of high and low density clumps of equal grey opacity. The effective opacity was calculated with the same MC method as used in JEKYLL, and the limits using the expressions derived above. For the clump-like case shown in Fig. A.1 the clumps have equal size and the high density clumps a filling factor of 0.1. The optical depth differs by a factor of 1000 and the geometrical mean free path is ∼15 times larger than the size of the low density clumps. For the bubble-like case shown in Fig. A.2 the low density clumps are 20 times larger and have a filling factor of 0.1. The optical depth differs by a factor 100 and the geometrical mean free path is ∼15 times smaller than the size of the low density clumps.

As seen in the figures, in the clump/bubble-like case, the effective opacity follows the optically thick limit until the clump/bubble limit exceeds the optically thick limit. The effective opacity then temporary moves into the clump/bubble limit, where the opacity is only determined by the geometry, follows this path until the clump/bubble limit exceeds the optically thin limit, and then moves into the optically thin limit.

Finally, lets explore a case more similar to the SN models in this work. Beginning with a smooth medium with constant grey opacity we divide it in two types of clumps of the same size and with filling factors 0.9 and 0.1. We then expand the latter (while keeping the **average?** density constant) by a factor of 9 to achieve a filling factor of 0.9. This is in line with the values

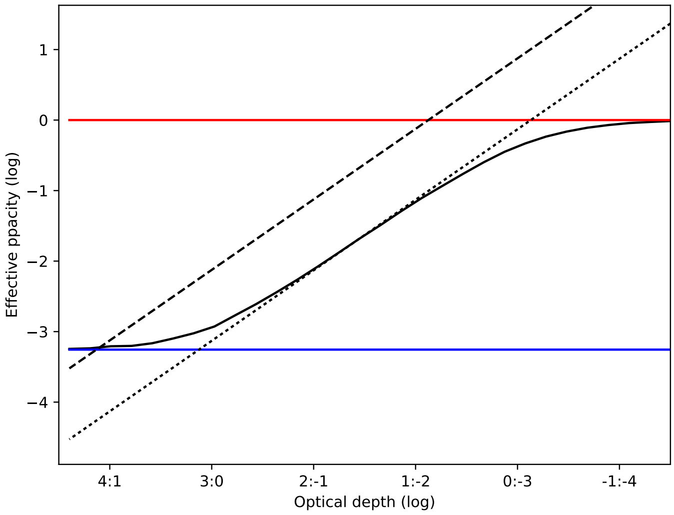

Fig. A.2. Effective opacity (black) for a homologously expanding bubble-like medium with high and low density clumps of equal opacity, where the low density clumps have a filling factor of 0.1 and are 20 times larger. We also show the optically thin (blue), optically thick (red) and geometrical clump (dashed black) and bubble (dotted black) limits. The opacity is given in arbitrary units, and the optical depth as H:L, where H and L are the optical depths in the high and low density clumps, respectively.

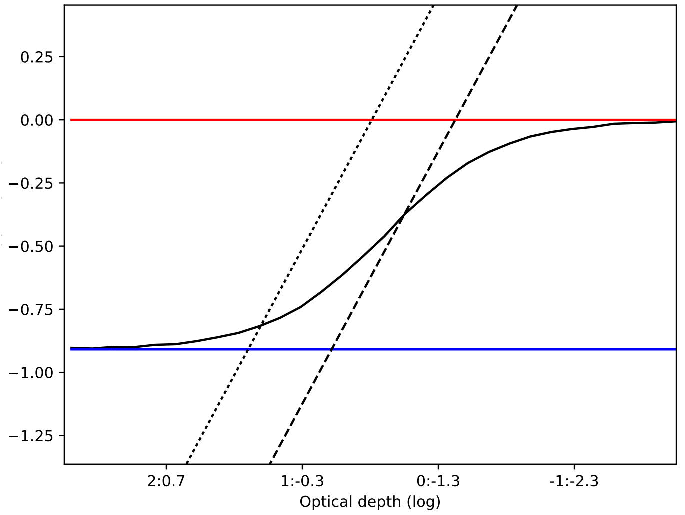

Fig. A.3. Effective opacity (black) for a homologously expanding medium with two types of clumps of equal mass and filling factors 0.9 and 0.1, where the latter have been expanded by a factor of 9. We also show the optically thin (blue), optically thick (red) and geometrical clump (dashed black) and bubble (dotted black) limits. The opacity is given in arbitrary units, and the optical depth as H:L, where H and L are the optical depths in the high and low density clumps, respectively.

for the Fe/He/Co zone in the core in the macroscopically mixed standard model. The optical depth differs by a factor of ∼20 and the geometrical mean free path is ∼3 times larger than the size of the low-density clumps, so the medium is modestly clump-like.

The calculated effective opacity and the corresponding limits are shown in Fig. A.3, and as seen, during the transition from the optically thick to the optically thin limit the effective opacity crosses both geometrical limits, but does not follow any of them, although it is skewed towards the clump limit. In the optically thin limit, the effective opacity equals that of a smooth medium, but from Eq. A.16 we see that in the optically thick limit it decreases by a factor

$$R = \Phi_C/f_C + \Phi_E\, f_E = \frac{(1-\Phi_E)^2}{(1-\Phi_E/f_E)} + \Phi_E\, f_E, \qquad (A.20)$$

where f_C is the compression factor for the high density clumps, f_E the expansion factor for the low density clumps, and we have used $\Phi_C = 1 - \Phi_E$ and $f_C = (1-\Phi_E/f_E)/(1-\Phi_E)$. This gives a decrease of the effective opacity by a factor of 9 for the numbers given in this example. The general dependence of the opacity decrease in the optically thick limit on the filling factor and expansion factor of the low density clumps is illustrated in Fig. A.4. From Eq. A.20 we see that the effective opacity can not decrease more than the clumps have been expanded. If the filling factor for the expanded clumps is large ($\Phi_E \approx 1$), the opacity decrease is given by $\Phi_E\, f_E$, and if it is small ($\Phi_E \approx 0$) by $1 + \Phi_E\, f_E$.

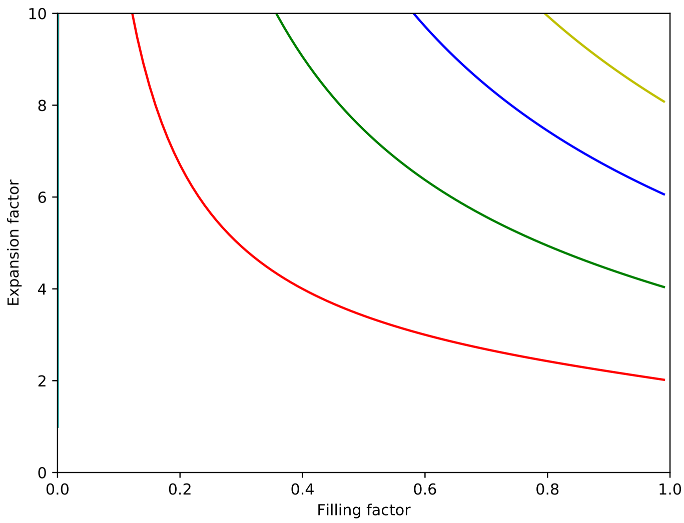

Fig. A.4. Effective opacity decrease in medium with uniform grey opacity, where one type of clumps have been expanded by a factor f_E to reach filling factor of Φ_E. Contours are shown for a decrease of the effective opacity by a factor of 2 (red), 4 (green), 6 (blue), and 8 (yellow).

References

Aldering, G., Humphreys, R. M., & Richmond, M. 1994, AJ, 107, 662
Bersten, M. C., Benvenuto, O. G., Nomoto, K., et al. 2012, ApJ, 757, 31
Dessart, L. & Audit, E. 2019, A&A, 629, A17
Dessart, L., Hillier, D. J., Li, C., & Woosley, S. 2012, MNRAS, 424, 2139
Dessart, L., Hillier, D. J., & Wilk, K. D. 2018, A&A, 619, A30
Dessart, L., Hillier, D. J., Woosley, S., et al. 2015, MNRAS, 453, 2189
Dessart, L., Hillier, D. J., Woosley, S., et al. 2016, MNRAS, 458, 1618
Ennis, J. A., Rudnick, L., Reach, W. T., et al. 2006, ApJ, 652, 376
Ergon, M. 2015, PhD thesis, Stockholm University
Ergon, M., Fransson, C., Jerkstrand, A., et al. 2018, A&A, 620, A156
Ergon, M., Jerkstrand, A., Sollerman, J., et al. 2015, A&A, 580, A142
Ergon, M., Sollerman, J., Fraser, M., et al. 2014, A&A, 562, A17
Fox, O. D., Azalee Bostroem, K., Van Dyk, S. D., et al. 2014, ApJ, 790, 17
Fransson, C. & Chevalier, R. A. 1989, ApJ, 343, 323
Fryxell, B., Mueller, E., & Arnett, D. 1991, ApJ, 367, 619
Herant, M. & Benz, W. 1991, ApJ, 370, L81
Jerkstrand, A., Ergon, M., Smartt, S. J., et al. 2015, A&A, 573, A12
Jerkstrand, A., Fransson, C., & Kozma, C. 2011, A&A, 530, A45
Jerkstrand, A., Fransson, C., Maguire, K., et al. 2012, A&A, 546, A28
Kozma, C. & Fransson, C. 1992, ApJ, 390, 602
Liu, Y.-Q., Modjaz, M., Bianco, F. B., & Graur, O. 2016, ApJ, 827, 90
Lucy, L. B. 1991, ApJ, 383, 308
Lucy, L. B. 2002, A&A, 384, 725
Lucy, L. B. 2003, A&A, 403, 261

Lucy, L. B. 2005, A&A, 429, 19
Marion, G. H., Vinko, J., Kirshner, R. P., et al. 2014, ApJ, 781, 69
Maund, J. R., Fraser, M., Ergon, M., et al. 2011, ApJ, 739, L37
Maund, J. R., Smartt, S. J., Kudritzki, R. P., Podsiadlowski, P., & Gilmore, G. F. 2004, Nature, 427, 129
Mueller, E., Fryxell, B., & Arnett, D. 1991, A&A, 251, 505
Shigeyama, T., Suzuki, T., Kumagai, S., et al. 1994, ApJ, 420, 341
Shull, J. M. & van Steenberg, M. 1982, ApJS, 48, 95
Stritzinger, M. D., Taddia, F., Burns, C. R., et al. 2018, A&A, 609, A135
Taddia, F., Sollerman, J., Leloudas, G., et al. 2015, A&A, 574, A60
Taddia, F., Stritzinger, M. D., Bersten, M., et al. 2018, A&A, 609, A136
Wongwathanarat, A., Janka, H.-T., Müller, E., Pllumbi, E., & Wanajo, S. 2017, ApJ, 842, 13
Woosley, S. E., Eastman, R. G., Weaver, T. A., & Pinto, P. A. 1994, ApJ, 429, 300
Woosley, S. E. & Heger, A. 2007, Phys. Rep., 442, 269